COMPUTATIONAL STUDIES OF GOLD-ADSORBATE COMPLEXES ON MODIFIED OXIDES

BY
JANNE NEVALAITA

Academic Dissertation
for the Degree of
Doctor of Philosophy

To be presented, by permission of the
Faculty of Mathematics and Natural Sciences
of the University of Jyväskylä,
for public examination in Auditorium FYS-1 of the
University of Jyväskylä on April 1st, 2016
at 12 o'clock noon

Jyväskylä, Finland
January 2016

Preface

The work presented in this thesis was done at the Nanoscience Center (NSC) of the University of Jyväskylä during the years 2012-2016.

I would like to thank my supervisors Dr. Karoliina Honkala and Professor Hannu Häkkinen for their guidance which has made this research possible. I would also like to thank Dr. Jenni Andersin for a motivating collaboration. A big thank you for Dr. Vesa Apaja for always being helpful in solving computer related technical issues. I would like to thank the reviewers Professor Núria López and Professor Kai Nordlund for their valuable comments. Further I want to thank Dr. Andre Clayborne for a thorough language revision. For interesting discussions about research and science in general, I would like to thank Professor Robert van Leeuwen, Dr. Sami Malola, M.Sc. Markku Hyrkäs, M.Sc. Ville Härkönen, M.Sc. Mauri Jauhiainen, M.Sc. Vesa Pitkänen, M.Sc. Sakari Tuokko, M.Sc. Riku Tuovinen, and Mr. Ville Ari. I would also like to thank all the people at the NSC and Department of Physics for creating a friendly working environment.

Finally, I would like to thank my family and friends, especially my parents Merja and Eero, and my brother Joonas for their encouragement. Most of all, I am thankful to my lovely fiancée Marjo-Leea for the invaluable support during this work.

Jyväskylä, March 2016

Janne Nevalaita

Abstract

While bulk gold is known for its chemical inertness, nanosized gold clusters are active catalysts for a variety of important reactions. For some practical applications gold clusters are supported and the cluster-support interaction can modify the cluster's properties. The knowledge of this interaction can be vital for obtaining desired cluster properties. In this thesis, the adsorption of Au atoms and clusters on modified oxide surfaces is studied using density functional theory (DFT) calculations. The support effects are considered by direct analysis of the adsorbed Au and using other coadsorbates as reactivity probes.

Doping the CaO(001) surface by replacing a cation with a high valence dopant such as Mo makes adsorption of electronegative species such as Au, O and O_2 more exothermic. The stronger binding is accompanied with a charge transfer from the dopant to the adsorbate. An Au adatom is anionic on a doped oxide as seen from its Bader charge and zero magnetic moment. The charging of the dopant is seen from a PDOS analysis where some of the d-electrons of the dopant are transferred to the Au s-states. Further, the change of the dopant's charge can also be seen by the contraction of the nearest neighbour distances between the dopant and surrounding O anions shows the change in the dopant charge. The superoxo state of O_2 on Mo doped CaO(001) is illustrated by its elongated bond length in addition to the Bader charge and magnetic moment of the molecule.

A modified Born-Haber (BH) cycle was devised to estimate the effect of different physical processes on the adsorption energy on the doped oxide. The adsorption energy was split into three parts with an iono-covalent energy describing the local interactions, a redox energy accounting for the charge transfer, and a Coulomb energy for the electrostatics between a charged adsorbate and dopant. While the Coulomb energy decays with increasing adsorbate-dopant distance, the redox energy remains more exothermic due to a much shorter distance between the negative anions and the positive dopant. A similar BH cycle for Ag(001) supported MgO thin films showed that while the electrostatic stabilization from the adsorbate-support interaction decays quickly with increasing film thickness, a compensation occurs in the redox energy becoming more exothermic, leading to more exothermic adsorption also for thicker films.

Water is stabilized by electrostatic interaction with anionic Au on MgO/Ag(001); however, no stabilization occurs on bulk MgO when the Au adatom is neutral. The adsorption of water dissociation products H and OH on top of an Au adatom is more exothermic with increasing film thickness. Isophorone physisorbs on the MgO/Ag(001) surface with energetic preference towards the MgO steps, which is due to stabilizing electrostatic interaction between the step cations and a polar O=C bond in the molecule. The enol tautomers can bind to anionic Au atoms on the surface via a similar interaction with the polar H-O bond. The keto form is not stabilized by Au due to a steric hindrance caused by C atoms near the positive end of the polar O=C bond.

Author's address   Janne Nevalaita
Nanoscience Center
Department of Physics
University of Jyväskylä
Finland

Supervisors   Docent Karoliina Honkala
Nanoscience Center
Department of Chemistry
University of Jyväskylä
Finland

Professor Hannu Häkkinen
Nanoscience Center
Department of Physics and
Department of Chemistry
University of Jyväskylä
Finland

Reviewers   Professor Núria López
Institute of Chemical Research of Catalonia
The Barcelona Institute of Science and Technology
Spain

Professor Kai Nordlund
Division of Materials Physics
Department of Physics and
Helsinki Institute of Physics
University of Helsinki
Finland

Opponent   Associate Professor Anders Hellman
Competence Centre for Catalysis and
Department of Applied Physics
Chalmers University of technology
Sweden

List of Publications

I J. Andersin, J. Nevalaita, K. Honkala, and H. Häkkinen, *The Redox Chemistry of Gold with High-Valence Doped Calcium Oxide* Angew. Chem. Int. Ed. **52**, 1424 (2013)

II J. Nevalaita, H. Häkkinen and K. Honkala, *Dissociative adsorption of water on Au/MgO/Ag(001) from first principles calculations* Surf. Sci. **640**, 10 (2015)

III J. Nevalaita, H. Häkkinen, and K. Honkala *Gold assisted oxygen dissociation on a molybdenum-doped CaO(001) surface* Catal. Sci. Tech., DOI: 10.1039/c5cy01839k

IV J. Nevalaita, K. Honkala, and H. Häkkinen *Isophorone on Au/MgO/Ag(001): Physisorption with electrostatic site selection* Manuscript

The author has done all of the numerical calculations and written the first drafts of articles **II**, **III** and **IV**. The author has also done the computations for systems with dopants other than Mo and participated in writing of the article **I**.

Contents

Abbreviations

BEEF	Bayesian error estimation functional
BH	Born-Haber
DOS	Density of states
DFT	Density functional theory
GGA	Generalized gradient approximation
GPAW	DFT code based on real space grids and PAW formalism
HOMO	Highest occupied molecular orbital
KS	Kohn-Sham
LDA	Local density approximation
LDOS	Local density of states
LSDA	Local spin-density approximation
LUMO	Lowest unoccupied molecular orbital
ML	Monolayer
QW	Quantum well
PAW	Projector augmented wave (method)
PBE	Perdew-Burke-Ernzerhof (XC functional)
PDOS	Projected density of states
STM	Scanning tunneling microscopy
vdW	van der Waals
XC	Exchange and correlation

1 Introduction

1.1 Metal oxides, oxide thin-films, and doped oxides

Metal oxides are a large and versatile group of materials with a broad range of applications in both industry and basic research. They are used for example in electronics, protective coatings, bio-compatible materials, and heterogeneous catalysis [1–7]. Their properties vary from chemically inert wide band gap insulators to chemically active species. Metal oxides are formed by metal atoms bound to oxygen, and the same metal can form multiple oxides depending on the ratio of oxygen to metal. For example, Cu can form either CuO or Cu_2O oxide depending on the ratio of oxygen to copper. These oxides have different atomic structures and different formal charges of the Cu cations. For CuO, the Cu charge is +2 and for Cu_2O it is +1. Oxides can be broadly divided into two categories, namely non-reducible and reducible oxides. The non-reducible simple oxides such as MgO and CaO are formed from alkali earth metals and they are usually chemically inert. On the other hand, the reducible oxides such as TiO_2 and FeO are formed from transition metals and are in general more reactive. The difference in reactivity between these oxide types makes them suitable for different applications. Reducible oxides are used as catalysts, since their higher reactivity allows them to bind species or act as a source of oxygen. The simple oxides, however, are used for example as passive supports. Metal oxide surfaces can exhibit highly different atomic structure from the bulk structures, in particular for reducible oxides. The atoms on the oxide surface rearrange to minimize the Gibbs free energy and depending on the material these rearrangements can yield significant changes when compared with the bulk structure. Interestingly, some simple oxides such as MgO and CaO, on the other hand, do not exhibit surface reconstruction and their surfaces remain the same as their bulk structures. The chemical properties of simple oxides are dominated by surface defects that can be reactive. For example it is known from computational studies that step sites on MgO(001) can dissociate water without a reaction barrier [8]. In this thesis, I focus on simple oxides with two modifications, namely doping and thin film arrangement, which are discussed next.

Properties of simple oxides can be modified by using them in a thin film arrangement. Here, the simple oxide is grown on a support metal to the desired thickness that can be as thin as a single monolayer. The properties of these thin film surfaces can be vastly different from bulk oxides and the difference is controllable by altering the film thickness. While ultra thin films of only a few monolayers exhibit altered

1

properties from the bulk, by growing the film thicker the bulk behaviour can be restored [9]. Since the film thickness can be controlled to an atomic precision, the desired surface can be achieved by tuning the film thickness. Additionally, since the simple oxides are wide gap insulators they are not accessible to certain local surface science techniques, namely scanning tunneling microscopy [10]. Contrary to the bulk, the thin film arrangement can be probed by STM since the tunneling current can pass through the thin oxide film. This allows the experimental study of local properties such as adsorbates and defects on the surface.

The properties of simple oxides can also be altered with doping [7, 11–14]. Replacing some of the cations of a simple oxide with different metal can lead to large variations in the properties of the oxide. Introducing for example Mo atoms into a CaO lattice in a concentration of about one percent makes the CaO surface reactive towards adsorbing electronegative species such as Au and O_2 [15]. This is due to introduction of d-state electrons of Mo, which lie in the CaO band gap and can be donated to electronegative adsorbates on the surface. Note that the dopant concentration can have profound effects on the material, and thus provides an additional and highly controllable parameter for materials design. Doping can further be used to change the defect concentrations of simple oxides since the O vacancy formation energy changes greatly when dopants are introduced. In realistic systems, oxides form compensating defects to remain charge neutral when electron rich or poor dopants are introduced. The inclusion of electron rich dopants leads to the formation of O vacancies or F-centers, where the extra electrons can be trapped, while electron poor dopants can lead to cationic vacancies that provide the equivalent traps for holes [16].

1.2   Gold as a catalyst

Gold is a noble metal and has been known since ancient times. Due to its fascinating color and easy malleability, it is a desired material for jewelry and decoration. In more modern times, the good electrical conductivity together with gold's resistance against corrosion made it to be widely used in electronics applications [17, 18]. Since bulk sized gold interacts weakly with oxygen, it was thought to be a poor catalyst compared with platinum group metals [19]. While it is true that bulk gold is chemically inert, the chemical activity increases significantly for nanosized gold particles roughly below the three nanometer size scale [20]. The current interest in gold as a catalyst can be traced back to two observations in the 80's [21, 22], even tough some hints of gold's chemical activity were already present in earlier studies [23]. First, in 1985 Hutchings predicted that Au^{3+} would be an optimal catalyst for ethyne hydrochlorination, which was confirmed later [24–26]. Secondly, supported Au catalysts were found to be very active in oxidizing CO at low temperatures [27]. After these findings gold has also turned out to be a potential catalyst for multiple additional reactions

including hydrogenation of CO and CO_2 to methanol, the water-gas shift reaction, and reduction of NO by hydrogen, propene or CO [28]. The catalytic activity of gold has been a subject of multiple studies. For example, the CO oxidation as catalyzed by gold has been investigated with theoretical and experimental means both in the gas-phase [29–32] and on multiple supports, such as TiO_2 [33, 34] and MgO [35–37].

The interesting chemical properties of gold can be connected to its electronic properties [38]. Since Au is a heavy element, it has inner electrons with high kinetic energies and electrons with high energies exhibit relativistic effects. Since all electron orbitals need to be orthogonal, changes in the inner orbitals due to their relativistic nature alter the properties of the valence electrons. More specifically, the 6s valence orbitals of Au are stabilized and contracted, leading to an increased screening of the nuclear charge for the d orbitals, expanding and destabilizing them. This makes sd hybridized states easily accessible and leads to highly directional bonding for Au atoms. These effects are particularly pronounced for Au, since the amount of contraction for the 6s orbital has a clear maximum at proton number 79, corresponding to Au [39]. The stabilization of the 6s orbital has a profound effect also on the electron affinity of gold as well. The relativistic contribution to the electron affinity of gold has been calculated to be 1.03 eV while it is only 0.07 and 0.22 eV for the other noble metals Cu and Ag, respectively [40]. The preference for planar geometry in small gold clusters with fewer than about ten atoms has been connected to relativistic effects, namely the sd hybridized states in Au. This has been illustrated using DFT calculations that show by using relativistic corrections planar structures are energetically favored over 3D ones [41, 42].

1.3   Oxide supported gold atoms and clusters

Gold has high electronegativity and is easily charged on oxide thin films [43–45] and doped oxides with electron rich donors [46, 47]. The negative charging of a single Au atom on MgO thin film supported by Mo(001) was computationally predicted [43] and later confirmed with STM measurements [45]. The Au atoms form ordered structures on MgO/Ag(001) due to Coulomb repulsion, preventing the sintering of Au adatoms into larger clusters at very low temperature. A similar result was found for Au atoms on FeO/Pt(111) in a combined experimental and computational study [48], but with cationic Au-adatoms. The charging of Au is accompanied with a much stronger binding to the thin film compared with the bulk oxide. This increase in binding strength between Au atoms and the thin film surface leads to changes in the Au cluster morphology. While some vacuum clusters prefer 3D geometries, clusters on MgO/Ag and MgO/Mo surfaces grow into 2D structures with quasi hexagonal shape and the Au(111) lattice structure [49]. These 2D clusters have Quantum Well (QW) like states that have been measured with STM and simulated with DFT [50–

53]. These states correspond to the states of a 2D Harmonic Oscillator (HO) where the number of radial and angular nodes depend on the number of electrons confined in the harmonic potential. Similarly, Au clusters consisting of three to six atoms grow into linear chains on MgO/Mo and have analogous QW states, but this time corresponding to the 1D HO [54, 55]. These linear Au chains have been observed in STM experiments on MgO/Ag [54].

Interestingly, a similar change in Au cluster morphology was observed on Mo doped CaO(001) surface [46, 47]. While Au grew into 3D shapes on a thick CaO film, the Au clusters grew into 2D structures with quasihexagonal shapes on thinner films. Again computations showed that a similar charging effect was responsible for the change in the cluster morphology. The electron rich Mo dopants donate charge for the electronegative Au atoms, leading to stronger adhesion between the cluster and surface and thus favoring the 2D structure.

1.4   About this thesis

In this thesis, I used GGA-level computational density functional theory as implemented in the GPAW code [56, 57] mainly with the PBE Exchange and Correlation functional [58] together with appropriate extensions, namely DFT+U [59–61] and DFT+vdW [62], when needed. I studied the coadsorption of oxygen, water, and isophorone with Au adatoms on two different modified simple oxide surfaces with references to bulk oxides as applicable. The studied thin film arrangement is Ag(001) supported MgO, with thicknesses between one to three atomic layers. The simple doped oxide is Mo doped CaO(001), with comparisons computed with different high valence dopants such as Cr. The adsorption of oxygen is considered on a Mo doped CaO(001) surface, and the adsorption of water and isophorone on an Ag(001) supported MgO thin film. The focus is on the atomic and electronic structures, energetics, and charge states of Au and adsorbates.

This thesis is organized as follows: In Chapter 2 a brief introduction to the basic concepts of density functional theory are discussed, with some of the issues in the numerical implementation of the theory, and an overview of the analysis methods used. The results obtained in this thesis are discussed in Chapter 3. In Chapter 4 the results are summarized and presented with an outlook for possible future work.

2 Density functional theory

Density functional theory (DFT) is a widely used approach in computationally simulating the properties of atoms, molecules, surfaces, and bulk materials [63, 64]. The foundations of DFT have been laid out already in the sixties [65] in two papers, the first by Hohenberg and Kohn [66] and the second by Kohn and Sham[67]. Walter Kohn was awarded Nobel prize in chemistry for his work on DFT in 1998 [68]. DFT is the subject of many review papers [69–71] and textbooks [72]. In this chapter, a brief overview of the theoretical background is given.

2.1 Theory overview

2.1.1 The many-body problem and electronic Hamiltonian

The quantum mechanical description of a system is given by the Schrödinger equation

$$\hat{H}\Psi = E\Psi \tag{2.1}$$

where $\hat{H}$ is the Hamiltonian operator, Ψ is the wave function and E is the energy of the state Ψ. For a full quantum description of matter, the Hamiltonian should include terms for the kinetic energies of the nuclei and nuclei-nuclei interactions, but in many applications the desired accuracy can be obtained by treating only the electrons with a quantum mechanical description while considering the nuclei classically. This is known as the Born-Oppenheimer approximation and its success can in part be attributed to the fact that even the lightest nuclei are three orders of magnitude heavier than the electrons. For this discussion, the nuclei can be considered as point charges giving rise to an external potential $v(\boldsymbol{r})$ that affects the electrons. For a system with M nuclei

$$v(\boldsymbol{r}) = \sum_{I=1}^{M} \frac{Z_I}{|\boldsymbol{r} - \boldsymbol{R}_I|} \tag{2.2}$$

where Z_I and $\boldsymbol{R}_I$ are the charge and the position vector of the nucleus I, respectively. Note that atomic units are used throughout this chapter. The total energy E_{tot} is then

the sum of the energy of the electrons E in the external potential and the repulsion between the nuclei E_{II} given by electrostatics. The Hamiltonian for the electrons is

$$\hat{H} = \hat{T} + \hat{W} + \hat{V} \tag{2.3}$$

where $\hat{T}$ gives the kinetic energy of the electrons, $\hat{W}$ describes the two-body interaction between electrons and $\hat{V}$ gives the energy due to external potential. More explicitly, for N electrons interacting via Coulomb interaction

$$
\begin{aligned}
\hat{T} &= -\sum_{i=1}^{N} \frac{\nabla_i^2}{2} \\
\hat{W} &= \frac{1}{2} \sum_{i \neq j}^{N} \frac{1}{|\boldsymbol{r}_i - \boldsymbol{r}_j|} \\
\hat{V} &= \sum_{i=1}^{N} v(\boldsymbol{r}_i)
\end{aligned}
\tag{2.4}
$$

where $\boldsymbol{r}_i$ is the position vector of electron i. There are still problems in applying this into practical calculations which is clear when considering the values of the wave function in the position basis. They are given as a function of the position $\boldsymbol{r}$ and spin variable σ for each of the electrons $\Psi = \Psi(\boldsymbol{r}_1\sigma_1, \ldots, \boldsymbol{r}_N\sigma_N)$; therefore, the many-body wave function Ψ has $3N$ degrees of freedom in addition to the spin degrees of freedom. Note that increasing the number of degrees of freedom increases the memory requirements exponentially. This means that even if one would somehow be able to solve the Schrödinger equation, already the storing of the wave function would take a ridiculous amount of space (even for systems with a rather modest number of electrons). In practice, however, the measurable quantities and not the wave function, of the system are of substantial interest. These are represented by Hermitean operators $\hat{O}$ and their expectation values give the measured or observed values O. For example, the expectation value of $\hat{H}$ gives the energy E. Further, note that the expectation value of $\hat{V}$ is actually a simple functional of the electron density $(n(\boldsymbol{r}))$, which only has three degrees of freedom no matter how many electrons there are in the system. Unfortunately, the expectation value of the operator $\hat{T} + \hat{W}$ does not reduce to a functional of density with a direct calculation. However, in the next section it will be discussed that there is a density functional for the expectation value of $\hat{T} + \hat{W}$ for the state with the lowest energy, i.e. the ground state.

2.1.2 The Hohenberg-Kohn theorems and Kohn-Sham construction

The ground state of a quantum system Ψ_0 can be defined as the state with the energy E_0 such that $E_0 \leq E_n \; \forall n$, that is to say that the ground state is the state or states with the lowest energy. There can be multiple states with energy E_0 in which case the ground state is said to be degenerate. Degenerate ground states occur for example in open shelled atoms. Consider an arbitrary state χ which is assumed to be normalized for simplicity. It can be expanded in the eigenbasis of the Hamiltonian $\{\Psi_n\}$ with expansion coefficients c_n. Since the sum of the absolute squares of the expansion coefficients is unity one gets the equation

$$\langle \chi | \hat{H} | \chi \rangle \geq E_0. \tag{2.5}$$

Thus the ground state wave function minimizes the energy expectation value. Using this result, known as the Rayleigh-Ritz principle, Hohenberg and Kohn showed that there is a one-to-one correspondence between ground state density $n(\boldsymbol{r})$ and external potential $v(\boldsymbol{r})$ when neglecting the constant shifts of the potential and phase factors of the wave function [66]. This means that the ground state wave function is a functional of the electron density and therefore the ground state observables are also functionals of the density. The energy functional is

$$E[n] = F_{HK}[n] + \int \mathrm{d}\boldsymbol{r} v(\boldsymbol{r}) n(\boldsymbol{r}) \tag{2.6}$$

where the Hohenberg-Kohn functional is defined as

$$F_{HK}[n] = \langle \Psi[n] | \hat{T} + \hat{W} | \Psi[n] \rangle. \tag{2.7}$$

Note that the $F_{HK}[n]$ does not depend on the external potential $v(\boldsymbol{r})$, but the ground state energy does. Since there is a single ground state density for each external potential, the energy functional can be minimized with respect to the ground state density while holding the external potential fixed since the ground state density is a stationary point of the functional $E[n]$. Unfortunately the $F_{HK}[n]$ is not explicitly known. What is known is that the Hohenberg-Kohn functional describes the kinetic energies and interactions of electrons. Thus raising the question how $F_{HK}[n]$ can be approximated based on some practically solvable terms. There indeed is an approximation based on a non-interacting auxiliary system which can be solved numerically [67]. The idea is to use the fact that the Hohenberg-Kohn theorems did not restrict the two-body interaction, so it can be chosen freely. Consider the set of Hamiltonians

$$\hat{H}_\lambda = \hat{T} + \lambda \hat{W} + \hat{V}_\lambda \tag{2.8}$$

where the external potential $\hat{V}_\lambda$ is chosen so that the density corresponding to ground state Ψ_λ is equal for each value of λ i.e. $n(\boldsymbol{r}) = \langle \Psi_\lambda | \hat{n}(\boldsymbol{r}) | \Psi_\lambda \rangle \; \forall \lambda$, where $\hat{n}(\boldsymbol{r})$ is the density operator. There are two interesting cases. First, if $\lambda = 1$ one obtains the original Hamiltonian. Second interesting case is when $\lambda = 0$ giving a Hamiltonian without two-body interactions

$$\hat{H}_s = \hat{T} + \hat{V}_s[n]. \tag{2.9}$$

Note that due to nearly unique correspondence between external potential and density the potential $\hat{V}_s[n]$ is a functional of the ground state density of the original Hamiltonian, since there can be only one potential producing the density $n(\boldsymbol{r})$ in the non-interacting $\lambda = 0$ case. This Hamiltonian has eigenstate $\Phi_s[n]$, which is functional of the density and can be represented as a Slater determinant

$$\Phi_s(\boldsymbol{x}_1, \ldots, \boldsymbol{x}_N) = \begin{vmatrix} \phi_1(\boldsymbol{x}_1) & \cdots & \phi_1(\boldsymbol{x}_N) \\ \vdots & & \vdots \\ \phi_N(\boldsymbol{x}_1) & \cdots & \phi_N(\boldsymbol{x}_N) \end{vmatrix} \tag{2.10}$$

where the single particle states ϕ_n are solutions to the equation

$$\hat{H}_s \phi_n(\boldsymbol{x}_i) = \epsilon_n \phi_n(\boldsymbol{x}_i) \tag{2.11}$$

and $\boldsymbol{x}_i = \boldsymbol{r}_i, \sigma_i$ are the position and spin variables. The states ϕ_n can be obtained numerically relatively easily and with a variety of different methods. The energy expectation value for $\hat{H}_s$ is

$$E_s = \langle \Phi_s[n] | \hat{T} + \hat{V}_s | \Phi_s[n] \rangle = T_s[n] + \int \mathrm{d}\boldsymbol{r} v_s(\boldsymbol{r}) n(\boldsymbol{r}) = \sum_{n=1}^{N} \epsilon_n \tag{2.12}$$

where $T_s[n]$ is a well-defined kinetic energy functional of the density. Now the idea is to use the easy to solve states from the non-interacting Hamiltonian $\hat{H}_s$ to estimate the energy of the interacting system. This can be done by using the Hellmann-Feynman theorem

$$\frac{\partial E_\lambda}{\partial \lambda} = \langle \Psi_\lambda | \frac{\partial \hat{H}_\lambda}{\partial \lambda} | \Psi_\lambda \rangle. \tag{2.13}$$

Substituting the Hamiltonian $\hat{H}_\lambda$ and integrating both sides with respect to λ from zero to one gives

$$E - E_s = \int_0^1 \mathrm{d}\lambda \langle \Psi_\lambda | \hat{W} | \Psi_\lambda \rangle + \int \mathrm{d}\boldsymbol{r}(v(\boldsymbol{r}) - v_s(\boldsymbol{r}))n(\boldsymbol{r}). \tag{2.14}$$

Combining this result with equation (2.12) gives an expression for the energy of the interacting system

$$E = T_s[n] + \int_0^1 \mathrm{d}\lambda \langle \Psi_\lambda | \hat{W} | \Psi_\lambda \rangle + \int \mathrm{d}\boldsymbol{r}v(\boldsymbol{r})n(\boldsymbol{r}). \tag{2.15}$$

When this result is compared with equation (2.6), one notes that the F_{HK} functional is split into two parts. Further, the interaction between electrons has a large classical contribution that does not depend on λ which is known as the Hartree energy

$$U_H[n] = \int \mathrm{d}\boldsymbol{r}\mathrm{d}\boldsymbol{r}'\frac{n(\boldsymbol{r})n(\boldsymbol{r}')}{|\boldsymbol{r} - \boldsymbol{r}'|} \tag{2.16}$$

and it is given as a simple functional of the density. The Hartree energy can be used in part to account for the interactions and the remaining energy contributions are included in the exchange and correlation functional E_{XC}. The energy functional can now be expressed in terms of three simple functionals of the density and one complicated one $E_{XC}[n]$, remaining to be approximated

$$E[n] = T_s[n] + U_H[n] + V[n] + E_{XC}[n]. \tag{2.17}$$

2.1.3 Approximations for the Exchange-Correlation functional

Even though the energy contribution from the E_{XC} part of the energy functional is small when compared with the other terms in equation (2.17), it plays a very important role in the interactions between atoms. It is the dominant contribution to atomization energies and without it, atoms would bind very weakly or not at all [73]. Thus, the usefulness of the presented DFT scheme depends on the accuracy of the approximation

to the E_{XC} functional. Developing and testing XC functionals is a large research area in its own right and only few central points are considered in this section. Historically the first approximation for the E_{XC} was presented previously in the paper by Kohn and Sham. It is known as the Local Spin Density Approximation (LSDA). The idea is to use the spin densities $n_\uparrow(\boldsymbol{r})$ and $n_\downarrow(\boldsymbol{r})$ to estimate the exchange-correlation energy contribution locally at each point for the non-homogeneous system

$$E_{XC}^{LSDA}[n] = \int \mathrm{d}\boldsymbol{r} n(\boldsymbol{r}) g_{XC}(n_\uparrow(\boldsymbol{r}), n_\downarrow(\boldsymbol{r})) \tag{2.18}$$

where the energy density g_{XC} is that of a homogeneous electron gas with spin densities $n_\uparrow$ and $n_\downarrow$. In principle, the energy density g_{XC} needs to be obtained for each different spin density values $n_\uparrow(\boldsymbol{r})$ and $n_\downarrow(\boldsymbol{r})$ in the non-homogeneous system by calculating it for the homogeneous system with those densities. In practice the energy density is extracted from Monte Carlo simulations of homogeneous electron gas [74]. Note that the LSDA is exact for a homogeneous system, and thus one could assume that it is a good approximation only for a slowly varying density. However, it turns out that LSDA works well also for more rapidly varying density. The next step in approximating the exchange-correlation is to include the information about the local density variation via the gradient of the density. These approximations are known as Generalized Gradient approximations (GGA)

$$E_{XC}^{GGA}[n] = \int \mathrm{d}\boldsymbol{r} f(n_\uparrow(\boldsymbol{r}), n_\downarrow(\boldsymbol{r}), \nabla n_\uparrow(\boldsymbol{r}), \nabla n_\downarrow(\boldsymbol{r})) \tag{2.19}$$

Figure 2.1 shows a comparison between the calculated and experimental atomization energies of some diatomic molecules using both the LSDA and PBE XC functionals. Note the significant reduction in the overbinding when using the gradient corrected PBE functional. While the GGA level XC functionals improve the atomization energies from the LSDA description, there still are many well-known issues with the DFT description of certain materials.

2.1.4 Hubbard U correction

The DFT description of the electron-electron interaction included a Hartree term that causes the electrons to interact with fragments of its own charge [75]. The exact XC functional would cancel these effects but the approximate ones do not, especially the local or semi-local ones. The self-interaction leads to an unphysical delocalization of the electrons and makes metallic ground states more stable than they should be. This means that some systems are predicted to be metallic, while they are in fact
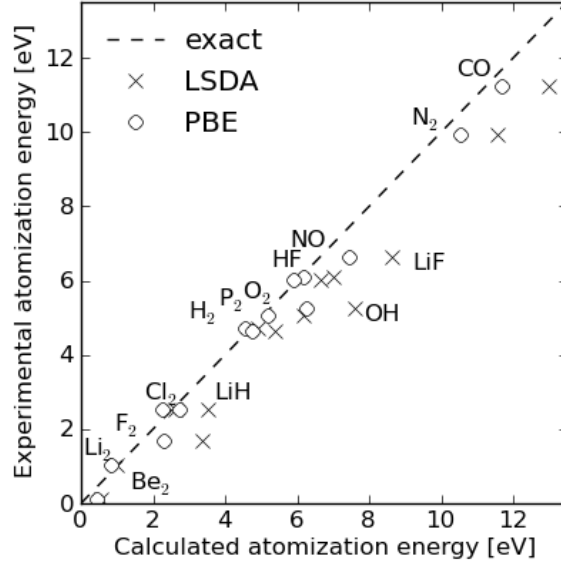
Figure 2.1: A comparison between experimental and calculated atomization energies for diatomic molecules using LSD and PBE XC functionals. Plot produced from data given in [58].

insulators. The error from delocalization is especially pronounced for the strongly localized d and f states of transition metals. A computationally inexpensive way of improving the description of these electrons is the inclusion of a so called Hubbard U correction. For the Hubbard U correction, some of the XC energy is substituted from the Hubbard model effective Hamiltonian to improve the description of localized states. Formally, this is done as

$$E_{\text{DFT+U}}[n] = E_{\text{DFT}}[n] + E_{\text{Hubbard}}[\{\psi_n\}] - E_{\text{dc}}[\{\psi_n\}] \qquad (2.20)$$

where $E_{\text{DFT}}[n]$ is the normal XC functional such as PBE, the $E_{\text{Hubbard}}[\{\psi_n\}]$ is a Hubbard correction and $E_{\text{dc}}[\{\psi_n\}]$ is a double counting term that should prevent the inclusion of the same density twice in the calculation of XC energy. Note that the Hubbard term and double counting term are functionals of the KS states $\{\psi_n\}$ and not just the electron density n. There are multiple ways of defining these terms and the one used in this thesis is perhaps the simplest where the DFT energy functional has an additional term depending on the occupation numbers of the atomic states that are corrected for unphysical delocalization

$$E_{\text{DFT+U}} = E_{\text{DFT}} + \frac{U}{2} \sum_a \text{Tr}(\rho^a - \rho^a \rho^a) \qquad (2.21)$$

where ρ^a is the atomic orbital occupation matrix and U is the Hubbard U parameter. The inclusion of the correction raises the energy for systems with states that are not completely occupied or unoccupied, thus giving an energy penalty for the delocalization of electrons.

2.1.5   van der Waals functionals

In practice, the binding energies are a result from the XC energies. However, the local and semilocal approximations do not capture the long range van der Waals interactions, which are important in the physisorption of molecules. [76]. Such a description of the van der Waals interaction of the system is achieved by including a nonlocal term in the XC functional

$$E_c^{\mathrm{nl}}[n] = \frac{1}{2} \int \mathrm{d}\boldsymbol{r}\mathrm{d}\boldsymbol{r}'n(\boldsymbol{r})\phi(\boldsymbol{r},\boldsymbol{r}')n(\boldsymbol{r}') \qquad (2.22)$$

where $\phi(\boldsymbol{r},\boldsymbol{r}')$ is the nonlocal interaction kernel. In this work, the BEEF XC functional [62] is used for systems where vdW interactions are deemed to be important.

2.2   Numerical methods

In this section, some aspects of the numerical methods used in this thesis are considered. All numerical calculations presented were done with the GPAW-code, which is a DFT implementation based on the usage of real space grids and PAW-formalism [56, 57].

2.2.1   Real space grids

To solve the Kohn-Sham equations computationally one needs a way to represent the wave functions and relevant operators in a numerical form. This can be done with an expansion to orthonormal basis functions φ_j and the expansion coefficients c_j are then saved for numerical representation. Consider the single particle eigenvalue problem

$$\hat{H}_s|\phi\rangle = \epsilon|\phi\rangle. \qquad (2.23)$$

This can be written as

$$\hat{H}_s \sum_j c_j |\varphi_j\rangle = \epsilon \sum_k c_k |\varphi_k\rangle. \tag{2.24}$$

Closing both sides with $\langle\varphi_i|$ from the left gives an eigenvalue equation

$$\sum_j H_{ij} c_j = \epsilon c_i \tag{2.25}$$

where the matrix elements H_{ij} are given by

$$H_{ij} = \langle\varphi_i|\hat{H}_s|\varphi_j\rangle \tag{2.26}$$

and the orthonormality of the basis functions has been used. By choosing suitable basis functions the matrix elements H_{ij}, can be calculated and the eigenvalue equation (2.25) can be solved to obtain the KS-orbitals in terms of basis functions φ_j and expansion coefficients c_j. Common choices for the basis functions are plane waves or localized atomic orbitals.

In this thesis, however, real space grids are used almost exclusively to represent the densities and KS-orbitals. In the real space grid representation, the values of functions are stored only in certain discrete points $\boldsymbol{g}$ on a grid $\mathcal{G}$. Consider functions $\varphi_{\boldsymbol{g}} : \mathcal{G} \to \mathbb{C}$ defined as $\varphi_{\boldsymbol{g}}(\boldsymbol{g}') = \delta_{\boldsymbol{g}\boldsymbol{g}'}$. Since every function on the grid is clearly a linear combination of linearly independent functions $\varphi_{\boldsymbol{g}}$, they form a basis. Further, the basis is orthogonal since $\langle\varphi_{\boldsymbol{g}}|\varphi_{\boldsymbol{g}'}\rangle = \Omega_{\boldsymbol{g}}\delta_{\boldsymbol{g}\boldsymbol{g}'}$ with respect to the inner product

$$\langle\psi|\phi\rangle = \sum_{\boldsymbol{g}\in\mathcal{G}} \Omega_{\boldsymbol{g}}\psi^*(\boldsymbol{g})\phi(\boldsymbol{g}) \tag{2.27}$$

where $\Omega_{\boldsymbol{g}}$ is the volume associated with the grid point $\boldsymbol{g}$ i.e., the volume of the set

$$g = \{\boldsymbol{r} \in \mathbb{R}^3 \mid \quad |\boldsymbol{r} - \boldsymbol{g}| \leq |\boldsymbol{r} - \boldsymbol{g}'| \quad \forall \boldsymbol{g}' \in \mathcal{G}\}. \tag{2.28}$$

Only values at certain discrete points $\boldsymbol{r}_G = (x_i, y_j, z_k)$ are saved, and interpolation methods are used to obtain values between the grid points. The calculation of expectation values and actions of derivative operators on real space grids warrant further discussion. Let us consider the KS-equations in a discrete form

$$[\nabla^2 \phi_n(\boldsymbol{r})]_{\boldsymbol{r}=\boldsymbol{r}_G} = 2(\epsilon_n - v_s(\boldsymbol{r}_G))\phi_n(\boldsymbol{r}_G) \tag{2.29}$$

and note that the Laplacian of the wave function ϕ_n needs to be represented in a discretized form. This is done by using finite differences to estimate the second order partial derivatives. With a central finite difference approximation the second order partial derivative with respect to x-coordinate in point $\boldsymbol{r}_G$ is given by

$$\left[\frac{\partial \phi_n(\boldsymbol{r})}{\partial x^2}\right]_{\boldsymbol{r}=\boldsymbol{r}_G} = \sum_{-m}^{m} c_m \phi_n(x_{i+m}, y_j, z_k) \tag{2.30}$$

where c_m are the finite difference coefficients depending on the grid and the order of expansion. Figure 2.2 shows a schematic 2D grid.
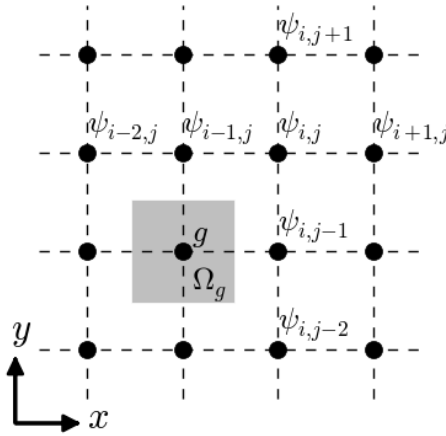

Figure 2.2: A schematic representation of a 2D grid showing a grid point $\boldsymbol{g}$ and the volume $\Omega_{\boldsymbol{g}}$ associated with $\boldsymbol{g}$ together with some values of a wave function ψ as represented on the grid.

2.2.2   Projector augmented wave method

While in principle the solutions to the one particle equations are obtainable by using the real space grid formalism described earlier, there still remains an important numerical issue. The used grid must be dense enough to capture the essential nodal structure of the wave functions, but sparse enough to have realistic memory requirements. A consideration of the physical properties of atoms in molecules and solids can be used to tackle this issue, namely, the fact that the wave functions have very different behaviours near the nuclei than further away from them. At the regions near the nuclei, the wave functions oscillate rapidly due to the large kinetic energy of the core electrons and the orthogonality requirement for the states. However, the electrons near the nucleus are not that sensitive to the chemical surroundings of the atom. Away from the nuclei, the valence states have smoother wave functions and a

strong dependence on the chemical environment. Using these observations, many ideas for numerically convenient ways to solve the one electron states have been proposed and implemented. For example, one could use denser grids near the nuclei to get an accurate description of the core electrons, while using sparser grids in the bonding regions to save on memory. Another way to make the problem more tractable is to use the insensitivity of the core electrons towards the chemical environment and treat them with a different method than the valence electrons. One could for example approximate that the nucleus and core electrons form an ionic core that has the same properties independently of the environment. Then treat only the valence electrons with a chosen method not in the potential due to nuclei, but in a potential due to these ionic cores. However, in this thesis a third approach is taken described below. The idea is to define a linear transformation between the true KS wave functions and computationally desirable pseudo wave functions. The linear transformation needs to be constructed only once and can then be used for all systems of interest. This method is known as the projector augmented wave (PAW) method [77, 78] and it is briefly described in this section. Figure 2.3 presents the idea schematically.
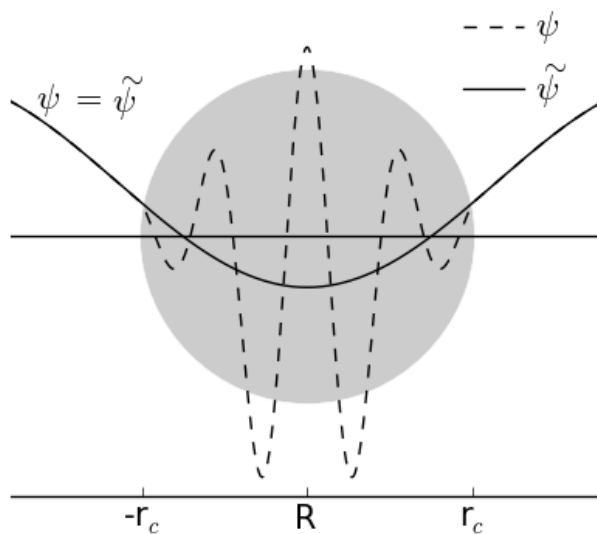

Figure 2.3: A schematic representation of the strongly oscillating true one electron wave function ψ and the corresponding smoother augmented wave function $\tilde{\psi}$ near an atom a at coordinates $\boldsymbol{R}$ with an augmentation sphere of radius r_c

Suppose that there is a Hilbert space of numerically convenient pseudo wave functions $\tilde{\psi}$ that can be connected to the real one electron states ψ via a linear transformation

$$|\psi\rangle = \hat{\mathcal{T}}|\tilde{\psi}\rangle. \tag{2.31}$$

Since the real wave functions behave smoothly outside of the nuclear regions, the

values of the pseudo wave functions can be the same as for the real functions in these regions

$$\psi(\boldsymbol{r}) = \tilde{\psi}(\boldsymbol{r}) \quad \text{when} \quad |\boldsymbol{r} - \boldsymbol{R}^a| > r_c^a \quad \forall \boldsymbol{R}^a, r_c^a \tag{2.32}$$

where $\boldsymbol{R}^a$ is the position vector and r_c^a is a cut off radius corresponding to atom a. The defined regions around each atom are known as augmentation spheres. Let's name the volume enclosed by them as Ω_A. By expanding the pseudo wave function inside the augmentation spheres, one gets

$$\tilde{\psi}(\boldsymbol{r}) = \sum_{a,i} c_i^a \tilde{\phi}_i^a(\boldsymbol{r}) \quad \boldsymbol{r} \in \Omega_A \tag{2.33}$$

where c_i^a are the expansion coefficients and $\tilde{\phi}_i^a$ are partial waves in the pseudo Hilbert space. Applying the linear transformation $\hat{\mathcal{T}}$ to the previous equation gives

$$\psi(\boldsymbol{r}) = \sum_{a,i} c_i^a \phi_i^a(\boldsymbol{r}) \quad \boldsymbol{r} \in \Omega_A \tag{2.34}$$

where ϕ_i^a are partial waves in the real Hilbert space obtained by the linear transformation $\hat{\mathcal{T}}$ from the states $\tilde{\phi}_i^a$. Since the expansion coefficients are the same in both expansions, the true one electron wave function can be written by combining the equations (2.33) and (2.34) as

$$|\psi\rangle = |\tilde{\psi}\rangle + \sum_{a,i} c_i^a (|\phi_i^a\rangle - |\tilde{\phi}_i^a\rangle). \tag{2.35}$$

Note that the previous equation defines the action of the linear transformation to the state $|\tilde{\psi}\rangle$. With this observation, the transformation can be written as

$$\hat{\mathcal{T}} = \hat{1} + \sum_{a,i} (|\phi_i^a\rangle - |\tilde{\phi}_i^a\rangle)\langle \tilde{p}_i^a| \tag{2.36}$$

where $\tilde{p}_i^a$ are so called projector functions, that satisfy

$$\langle \tilde{p}_i^a | \tilde{\psi} \rangle = c_i^a. \tag{2.37}$$

Further, by using the introduced expression for the expansion coefficients, equation (2.33) gives

$$|\tilde{\psi}\rangle = \sum_{a,i} |\tilde{\phi}_i^a\rangle \langle \tilde{p}_i^a|\tilde{\psi}\rangle \qquad (2.38)$$

which implies that

$$\sum_{a,i} |\tilde{\phi}_i^a\rangle \langle \tilde{p}_i^a| = \hat{1} \quad \text{and} \quad \langle \tilde{p}_i^a|\tilde{\phi}_j^b\rangle = \delta_{ij}\delta_{ab}. \qquad (2.39)$$

2.2.3 Periodic boundary conditions and relaxation geometries

Treating very large systems as infinitely or semi-infinitely large is a powerful approximation. For example, surface systems can be approximated to extend into infinity along the surface plane using the periodicity in the surface structure. When using the real space grid formalism, the periodic boundary conditions can be chosen independently in each direction. Atoms and molecules can be calculated with no periodicity in any direction, while the surface systems can be assumed to be periodic along the surface plane and non periodic parallel to the surface. The observables in periodic systems are calculated by applying Bloch's theorem to the KS states and then evaluating the energies in reciprocal space with a k-point grid.
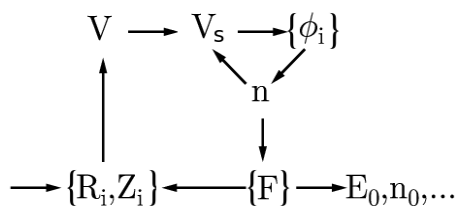

Figure 2.4: A schematic representation of a ground state calculation by two iterative circles.

The basic components needed for solving the ground of a particular system have been briefly explained in the previous sections. In practice, the solution is obtained by iteration, which is represented schematically in Figure 2.4. First, the system is specified by giving the coordinates and names of the atoms in the system. These specify the external potential, and with a suitable approximation for the XC functional, the single particle KS potential V_s is obtained. As the next step, the KS states $\{\phi_i\}$ corresponding to this potential are solved, and a new density is obtained from them. Using this density, a new KS potential is calculated and this cycle is then repeated until

self-consistency. This is now the ground state density of the system with the initially given coordinates. Using this density, the forces on the atoms can be obtained and new geometry constructed attempting to minimize these forces. The ground state density is then computed similarly for the new coordinates, until the forces are below a certain threshold value. Once the forces are below the threshold value, these coordinates are now called the relaxation geometry, from which the desired quantities, such as bond lengths, can then be extracted.

2.3   Analysis methods

As seen in the previous sections, DFT gives the relaxation geometry, the ground state energy, the ground state electron density and the KS-orbitals from a given external potential. In this section, the methods used to extract different information from these are discussed.

2.3.1   Density of states

The number of electronic states with energy ϵ is given by

$$g(\epsilon) = \sum_n \langle \psi_n | \psi_n \rangle \delta(\epsilon - \epsilon_n). \tag{2.40}$$

The local density of states can then be obtained by acting with the unit operator

$$g(\epsilon, \boldsymbol{r}) = \int \mathrm{d}\boldsymbol{r} \sum_n \langle \psi_n | \boldsymbol{r} \rangle \langle \boldsymbol{r} | \psi_n \rangle \delta(\epsilon - \epsilon_n). \tag{2.41}$$

The important qualitative differences in the density of states are more apparent when the density of states is projected onto well known basis functions such as the atomic orbitals. The projected density of states is given by

$$g(\epsilon) = \sum_n \langle \psi_n | \phi_i^a \rangle \langle \phi_i^a | \psi_n \rangle \delta(\epsilon - \epsilon_n). \tag{2.42}$$

In this work, the KS states are used to obtain DOS.

2.3.2 Density difference analysis

Adsorption is a process where an atom or a molecule, called an adsorbate, attaches to a surface. This is referred to as chemisorption if the species attaches to the surface with chemical bonding, or as physisorption if the adsorbate binds to the surface via van der Waals interaction. The change in the electron density in adsorption can be defined as

$$n_{\text{d.d.}} = n_{\text{adsorbate/surface}} - (n_{\text{adsorbate}} + n_{\text{surface}}) \tag{2.43}$$

where $n_{\text{adsorbate/surface}}$ is the electron density of the combined adsorbate on surface system, while $n_{\text{adsorbate}}$ and n_{surface} are the densities of adsorbate and surface with infinite separation. Note that all the electron densities are calculated with the atoms in the same positions as in the adsorbate on surface system, using the same computational cell. This is done to get the change in the electron density due to charge transfer between atoms, and not due to differences in relaxation geometries between the surface with and without the adsorbate. In many cases, the visualization of the charge transfer between different parts of the system can be done by studying the charge transfer along the surface normal. This can be done by defining the integrated density difference

$$n_{\text{i.d.d.}}(z) = \int \mathrm{d}x \mathrm{d}y n_{\text{d.d.}}(x, y, z) \tag{2.44}$$

where the z coordinate is perpendicular to the surface.

2.3.3 Bader charge decomposition

The output of a DFT simulation gives the ground state electron density, which contains the information of the locations of electrons in real space. However, describing charge transfer directly in terms of the electron density can be cumbersome, and therefore it is desirable to discuss the charges of individual atoms. The question then is how to associate electron density at a certain point with a certain atom, since there is no unique way of doing this. Within this thesis, the Bader charge analysis has been used since it provides an intuitive argument for dividing the electron density between atoms at a reasonably low computational cost within the real space grid implementation of DFT [79–82]. The electron density is divided by zero flux surfaces

$$\mathcal{S} = \{\boldsymbol{r} \in \mathbb{R}^3 \mid \nabla n(\boldsymbol{r}) \cdot \boldsymbol{u}(\boldsymbol{r}) = 0\} \tag{2.45}$$

where $\boldsymbol{u}(\boldsymbol{r})$ is the surface normal vector at point $\boldsymbol{r}$. The zero flux surfaces will divide the system into Bader volumes, where usually each atomic nucleus is contained in a single Bader volume. The Bader charge of an atom a is then

$$q_a = \int_{V_a} \mathrm{d}\boldsymbol{r} n(\boldsymbol{r}) + Z_a \tag{2.46}$$

where V_a is the Bader volume corresponding to a nucleus a with charge Z_a.

2.3.4 Total energy differences

An important quantity describing adsorption is the adsorption energy

$$E_{\mathrm{ads}} = E_{\mathrm{adsorbate/surface}} - (E_{\mathrm{adsorbate}} + E_{\mathrm{surface}}) \tag{2.47}$$

where the first term on the right hand side is the total energy of the surface with the adsorbate attached, and the latter two terms are the total energies of the adsorbate and surface with infinite separation. The adsorption energy is the energy stored or released when the adsorbate is brought on the surface from a vacuum infinitely far away. The sign of the adsorption energy is a matter of convention and both positive and negative signs for exothermic adsorption are used in the literature. For results discussed in this thesis, negative adsorption energy corresponds to exothermic adsorption.

2.3.5 Born-Haber cycle for adsorption

To evaluate the magnitude of the energy contributions of different physical processes, it can be useful to split the adsorption energy into multiple steps instead of just considering the initial and final states. In this work, a modified Born-Haber cycle is used for electronegative adsorbates on surfaces to estimate the energy contributions arising from local interactions, charge transfer, and electrostatic stabilization. This is done by dividing adsorption energy into three parts

$$E_{\mathrm{ads}} = E_{\mathrm{icov}} + E_{\mathrm{redox}} + E_{\mathrm{Coul}} \tag{2.48}$$

where each term is associated with a distinct physical process or interaction. The cycle is applied to two different oxide systems. For a doped CaO(001) oxide surface, the individual terms comprising the adsorption energy are defined as follows: The energy

associated with the iono-covalent interaction is defined as the adsorption energy on a pristine oxide surface

$$E_{\text{icov}} = E_{\text{X/CaO}} - (E_{\text{X}} + E_{\text{CaO}}) \tag{2.49}$$

where $E_{\text{X/CaO}}$ is the energy of the combined adsorbate on surface system, while E_{X} and E_{CaO} are the energies of the adsorbate and surface with infinite separation, respectively. This describes the local interaction between adsorbate and the adjacent surface atoms. The redox energy is defined as

$$E_{\text{redox}} = E_{\text{X}^-/\text{CaO}} + E_{\text{Ca(M}^{3+})\text{O}} - (E_{\text{X/CaO}} + E_{\text{Ca(M}^{2+})\text{O}}) \tag{2.50}$$

where $E_{\text{Ca(M}^{2+})\text{O}}$ is the energy of neutral M doped oxide, $E_{\text{Ca(M}^{3+})\text{O}}$ is the energy of doped oxide with one electron removed, and $E_{\text{X}^-/\text{CaO}}$ is the energy of adsorbate X on pristine CaO with one electron added to the system. The first two terms in the definition of E_{Redox} are calculated from charged systems, while the reference systems are neutral. Therefore, the redox energy term describes the effect of charge transfer to the adsorption energy. Finally, the Coulomb term is defined as

$$E_{\text{Coul}} = E_{\text{X}^-/\text{Ca(M}^{3+})\text{O}} + E_{\text{CaO}} - (E_{\text{X}^-/\text{CaO}} + E_{\text{Ca(M}^{3+})\text{O}}) \tag{2.51}$$

where $E_{\text{X}^-/\text{Ca(M}^{3+})\text{O}}$ is the energy of the adsorbate on the doped oxide. It is assigned to the Coulomb interaction between the negatively charged adsorbate and positive dopant. A similar cycle can be defined for the MgO/Ag(001) thin film arrangement.

3 Results

The main result in this thesis is that the metal supported simple oxide thin films and doped simple oxides can have analogous adsorption characteristics. Gold atoms and clusters display similar behaviour on both MgO/Ag(001) and high valence doped CaO having stronger surface adhesion and a more negative charge. A similar conclusion was recently obtained in an experimental STM study [83]. While the origin of the adsorbate charge is the support metal for the thin film arrangement, the dopants provide the charge on the doped surfaces. Both surfaces can also activate oxygen. In this chapter, the results presented in publications [I-IV] are discussed together with a brief summary of similar studies reported in literature.

3.1 The effect of oxide doping to the adsorption on CaO(001)

While the thin film arrangement of simple oxides is known to yield considerably different properties for adsorbates compared with the pristine bulk surfaces, the adsorption on doped oxides is yet to be as extensively studied. However, some features of the doped oxides are known. Experiments show that Au grows into 2D islands on a Mo doped CaO(001) surface, [46, 47] such as, on certain thin film arrangements. Computations predict that the change in Au-morphology is due to increased Au-surface adhesion, which is accompanied by the charging of the Au atoms, again in analogy to the thin film surfaces. Whereas the film thickness is a controllable parameter in the thin film arrangements, the dopant concentration is a new adjustable parameter for the doped oxides. The dopant concentration together with the choice of the oxide and dopant material can potentially be used to control the properties of oxide surfaces. In this section, the modification of the surface reactivity of CaO(001) oxide due to substitutional doping with high valence dopants is analyzed using Au and oxygen as reactivity probes.
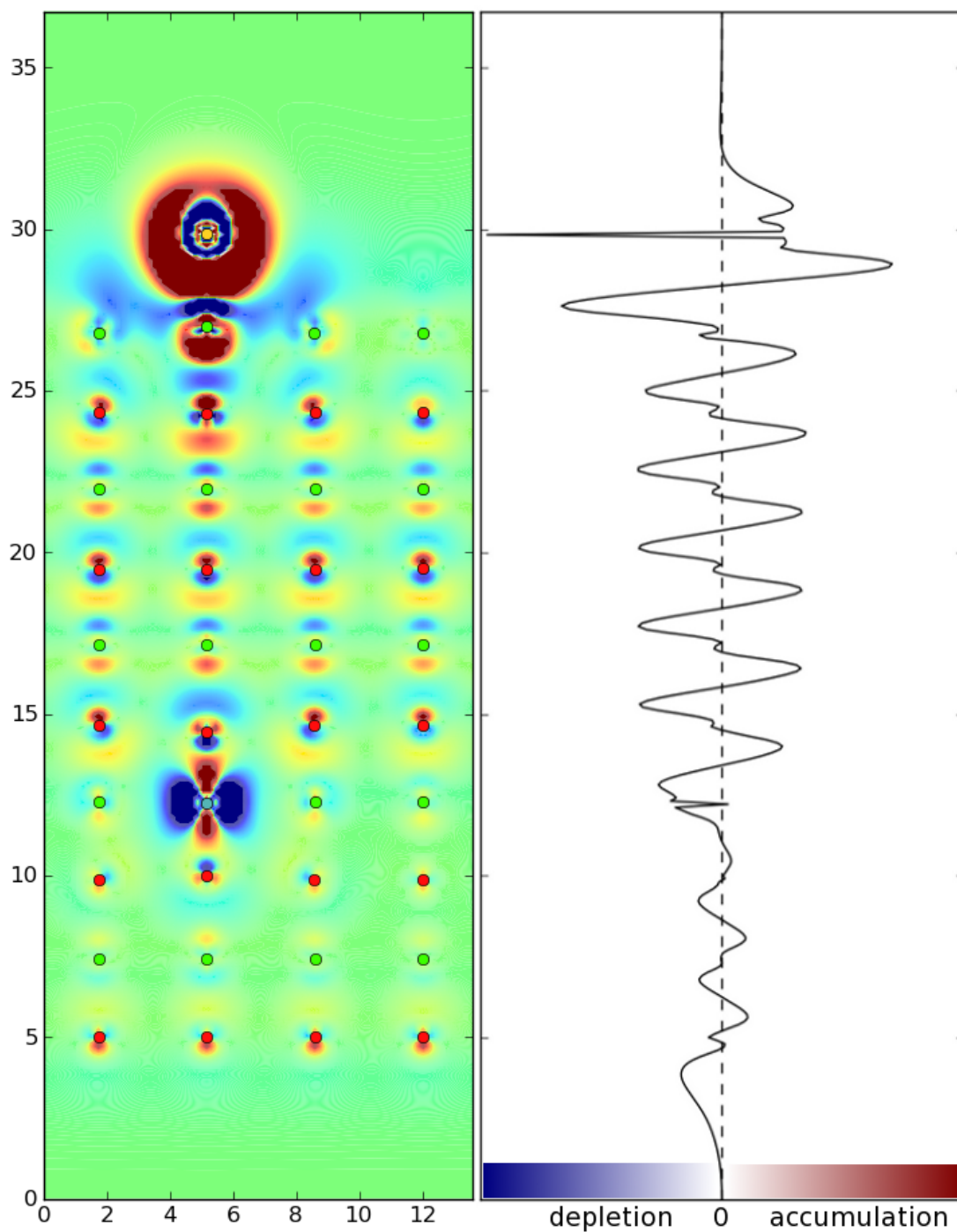
Figure 3.1: The density difference analysis of Au adsorption on Mo doped CaO(001). The left figure shows the density difference along a (110) plane with accumulation (depletion) of electrons shown in red (blue). The x-axis gives the distance in Å along the xy-plane and the locations of Au, Ca, Mo and O atoms are marked with yellow, green, blue, and red dots, respectively. The right figure shows the integrated density difference for the same system where the solid line to the left (right) of the dashed line indicates depletion (accumulation) of electrons in arbitrary units. The y-axis is the same for both plots and gives the z-coordinate in Å.
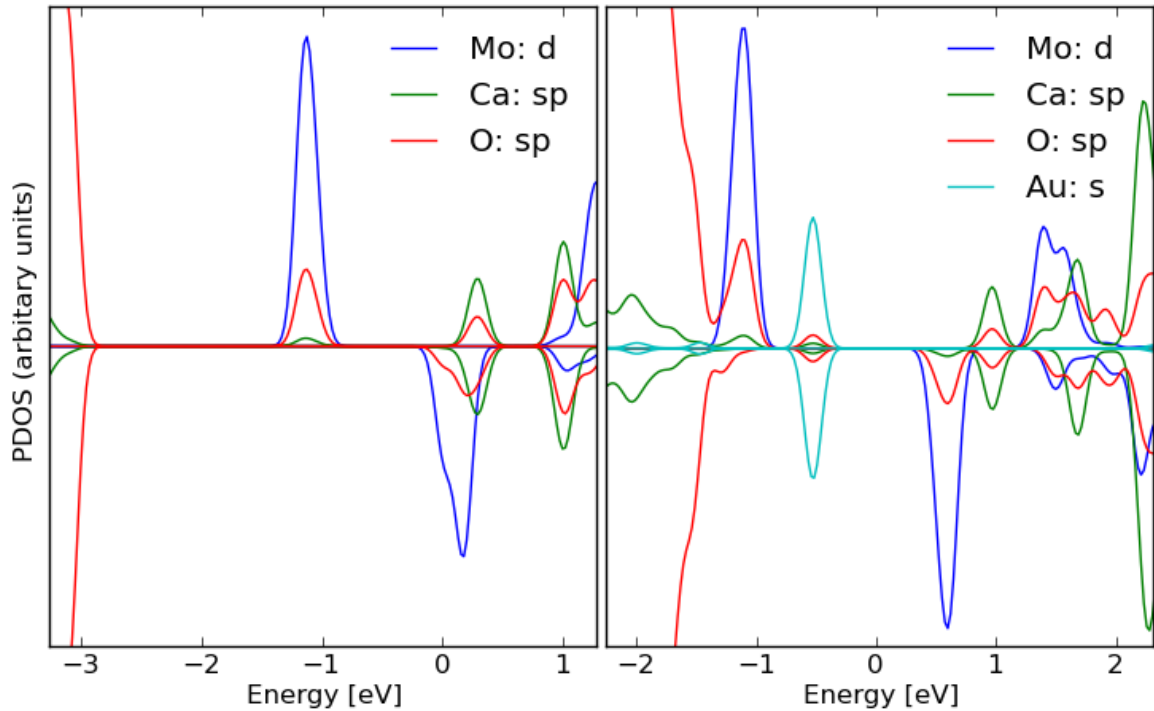
Figure 3.2: The PDOS of a Mo doped CaO(001) surface with and without an Au adatom projected onto the s, sp, and d orbitals of Au, CaO and Mo, respectively. The left (right) plot is for the surface without (with) the Au adatom. The Fermi level is set to zero in both plots.

3.1.1   Au adsorption on high valence doped CaO(001)

First, the Au adsorption on a pristine CaO(001) surface is considered, which will be used later as a comparison of adsorption on doped surfaces to fully analyze the effect of doping. The Au adsorption on an O-top site is energetically preferred over the Ca-top site by 0.8 eV. The stronger binding on the O-top site is not accompanied by charging of the Au atom. Instead a PDOS analysis shows that Au is charged on the Ca-top site, while it is neutral on the O-top site. The dopants are then introduced as substitutional impurities into an oxides lattice, where a Ca atom in the CaO oxide is replaced by a dopant atom. The choice of the dopant site is motivated by the experiments [84]. A sufficiently thick slab is needed to analyze the effect of dopant placement in the oxide. The CaO slab studied throughout this section is ten layers thick. For doping, one Ca atom is changed at a time, which yields a dopant concentration of 1.25%. The binding of Au to the surface increases significantly when the CaO(001) is doped with Mo. However, the binding site preference towards the O-top site vanishes with the Ca-top site becoming isoenergetic. The Au adatom on the Mo doped surface is also charged on the O-top site with a Bader charge of about -0.8 |e|. A density difference plot for Au adsorption with the Mo dopant in the 7th layer of the CaO(001) slab is

presented in Figure 3.1 that shows the adsorbate charge originates from the dopant. The charge transfer is accompanied with a formation of a polarization pattern that is very similar to the pattern reported for Au adsorption MgO/Mo(001) thin films [44].
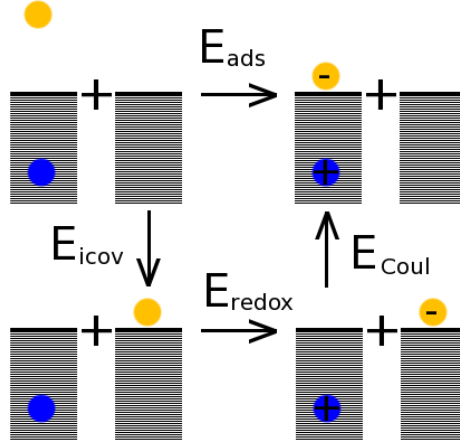

Figure 3.3: A schematic representation of the modified Born-Haber cycle used to split the adsorption energy into contributions E_{icov}, E_{redox}, and E_{Coul}.

The electronic origin of the charge transfer is due to the introduction of new states in the band gap of the oxide from doping. These gap states are partly occupied by the d-electrons of the high valence Mo and can be accepted by an adsorbate with high electronegativity. In Figure 3.2, the Mo d-states are shown before and after Au adsorption for Mo dopant. The charge transfer can be seen by considering the Mo d-states near the Fermi energy and the Au s-states. While the Mo d-states with energies near -1 eV are not affected by the adsorption, the states near the Fermi level on the left plot are partly occupied without the Au adatom; however, they are completely unoccupied and above the Fermi level with an Au adatom. This indicates an increase in the oxidation state of Mo. Further, the Au s-states show no spin polarization, but are symmetric for the spin up and spin down PDOS. This indicating that the Au atom is charged, since a neutral Au atom would have an unpaired 6s-electron. Some caution is advised here, when considering realistic systems that can have defects. Depending on the nature of these defect states, they can accept some of the Mo d-electrons thus, making them unavailable for adsorbates. However, increasing the dopant concentration should assure the availability of the dopant electrons for adsorbates. This will hold if the increase in concentration does not result in an equal increase in the charge trapping defects.

Based on the observed charge transfer and a Lewis acid-base interpretation, [85] we devise a scheme for splitting the adsorption energy into three distinct contributions, each connected with a certain physical process. The construction is shown schematically in Figure 3.3 and has been explained in more detail in section 2.3.5. The ad-
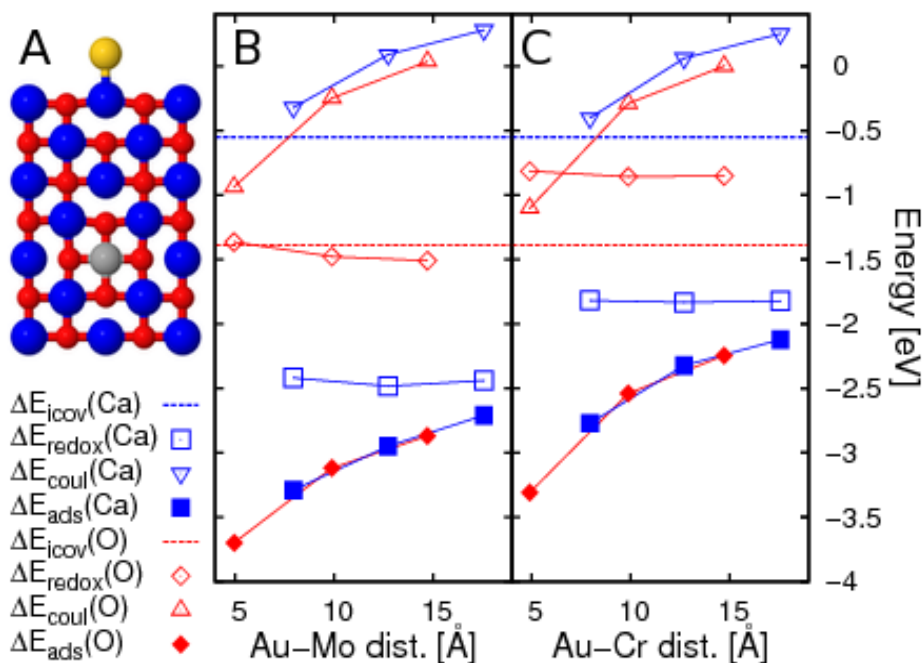
Figure 3.4: **A**: An example relaxation geometry for Au adsorption on doped CaO(001). Au is yellow, Ca is blue, dopant is grey, and O is red. **B**,**C**: The adsorption energy E_{ads} divided into three contributions E_{icov}, E_{redox}, and E_{Coul} defined in the text for Mo and Cr doped oxide shown in **B** and **C**, respectively.

sorption energy is divided into three parts where the energies describing the local iono-covalent adsorbate-surface interaction, the effect of the charge transfer, and electrostatic Coulomb interaction between adsorbate and dopant are obtained separately. The Au adsorption is then studied as a function of the dopant location, which is changed from the second most top layer to the seventh oxide layer while the adsorption site is always directly above the dopant.

The Au adsorption energy is significantly more exothermic on the doped oxides. This is seen by comparing the adsorption energy on doped oxides given by the full squares in Figure 3.4 (the adsorption energy on a pristine CaO(001) is given by the dashed lines). The origin of the increased reactivity, as suggested by the modified Born-Haber cycle, is in the redox effect. While the iono-covalent interactions can be significant on the O-top site (red plots), the redox term is clearly the leading energy contribution to the Ca-top site (blue plots). Typically, the redox energy dominates the Coulomb part of the adsorption energy. The significance of the redox energy can be rationalized in terms of simple electrostatics. While there is an attractive interaction between the negatively charged adsorbate and positive dopant, the distance between them is much larger than between the dopant and its neighbouring O^{2-} anions. Thus, the stronger attractive interaction between the CaO matrix and the dopant, due to the increase in

the positive charge of the dopant will dominate over the stabilization of the adsorbate by the attractive adsorbate-dopant interaction.
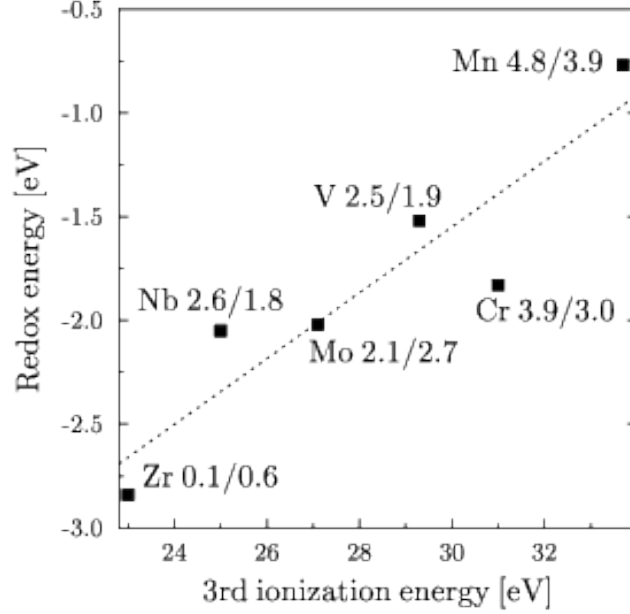

Figure 3.5: Correlation between the 3rd ionization potential of the dopant and the redox energy for six high valence dopants. Numbers given after the chemical symbol are the magnetic moments of the dopant in μ_B before and after adsorption, respectively. The ionization potentials are taken from [86].

Comparison between Mo and Cr doped CaO(001) shows a couple of interesting features. Firstly, the Coulomb contributions look nearly identical for Mo and Cr, that display an approximate $1/r$ dependence on the adsorbate-dopant distance, as expected for an electrostatic interaction between point charges. This is in agreement with the interpretation that the charge transfer is similar in both cases, and is indeed from the dopant to the adsorbate. Interestingly, the Coulomb energy has a small positive contribution in the long distance limit, contrary to the expected contribution of zero. This is due to the relaxations of the oxide ions, and is addressed in more detail in section 3.3.6. Secondly, the redox contributions appear to be similar but shifted to a higher energy by about 0.5 eV for the Cr dopant. This indicates that the surface reactivity could have a simple connection to the atomic properties of the dopant and indeed, it does. Figure 3.5 shows a correlation between the 3rd ionization potential of the dopant and the corresponding redox energy. The change in redox energy between dopants M_1 and M_2 is given by a direct calculation from the definition of the redox energy

$$\Delta E_{\text{redox}}^{M_1-M_2} = E_{\text{Ca}(M_1^{3+})\text{O}} - E_{\text{Ca}(M_1^{2+})\text{O}} - (E_{\text{Ca}(M_2^{3+})\text{O}} - E_{\text{Ca}(M_2^{2+})\text{O}}) \qquad (3.1)$$

where $E_{\mathrm{Ca(M}_i^q)\mathrm{O}}$ is the energy of a system with the dopant i at the charge state q. By considering the redox process in three steps, the correlation to the 3rd ionization potential can be rationalized. First, the 2+ ion is removed from the oxide with some associated vacancy formation energy. Then the 2+ ion is further ionized to 3+ and the energy required in this step is the 3rd ionization potential of the dopant. Lastly, the 3+ ion is placed back in the CaO vacancy. Since the vacancy formation and healing energies partly cancel each other and the energy required for the ionization from 2+ to 3+ is large, the redox energy becomes correlated to the ionization energy.
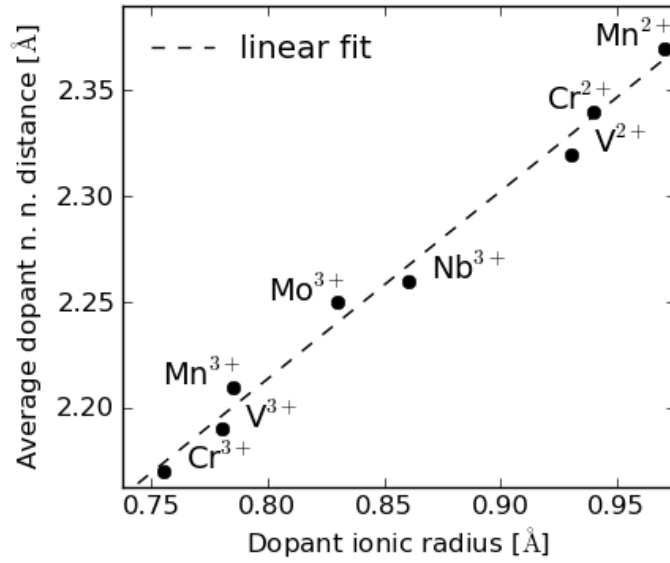

Figure 3.6: Correlation between the ionic radius of a dopant M and the average M-O^{2-} nearest neighbour distance. The ionic radii are taken from [87].

While the charging of an adsorbed Au atom can be confirmed by its vanishing magnetic moment and Bader charge analysis, the change in the dopants charge state is not always as evident from these methods. To further connect the charge obtained by Au as having originated from the dopant, a simple correlation between the charge and ionic radius of an atom can be utilized. The ionic radius decreases with an increasing oxidation state and this correlation can be connected to the dopant atoms by analysing the average distances between the dopants and their neighbouring O^{2-} anions. The dopant nearest neighbour distance correlates with the dopant ionic radii as shown in Figure 3.6. Thus, a change in the distance between dopant and adjacent O ions can be used as a further indicator of the change in the dopant oxidation state together with the PDOS analysis as shown in Figure 3.2.

3.1.2   Oxygen adsorption on Mo doped CaO(001)

Due to the general nature of the redox mechanism, one would expect similar results for another adsorbate with high electron affinity. This turns out to be the case for an O atom and the O_2 molecule. The relaxation geometries for oxygen adsorption on Mo doped CaO(001) surfaces are shown in Figure 3.7. It should be noted that we used the same ten layers thick CaO(001) slab as in the previous section, now with the Mo dopant in the 7th layer. A single O atom adsorbs on a Ca-top site while the oxygen molecule energetically favors the adsorption on a bridge site between two Ca cations. Though molecular oxygen barely interacts with a pristine CaO(001) surface, it has clearly exothermic adsorption energy, between -1.5 and -1.9 eV depending on the adsorption geometry, on the Mo doped oxide.
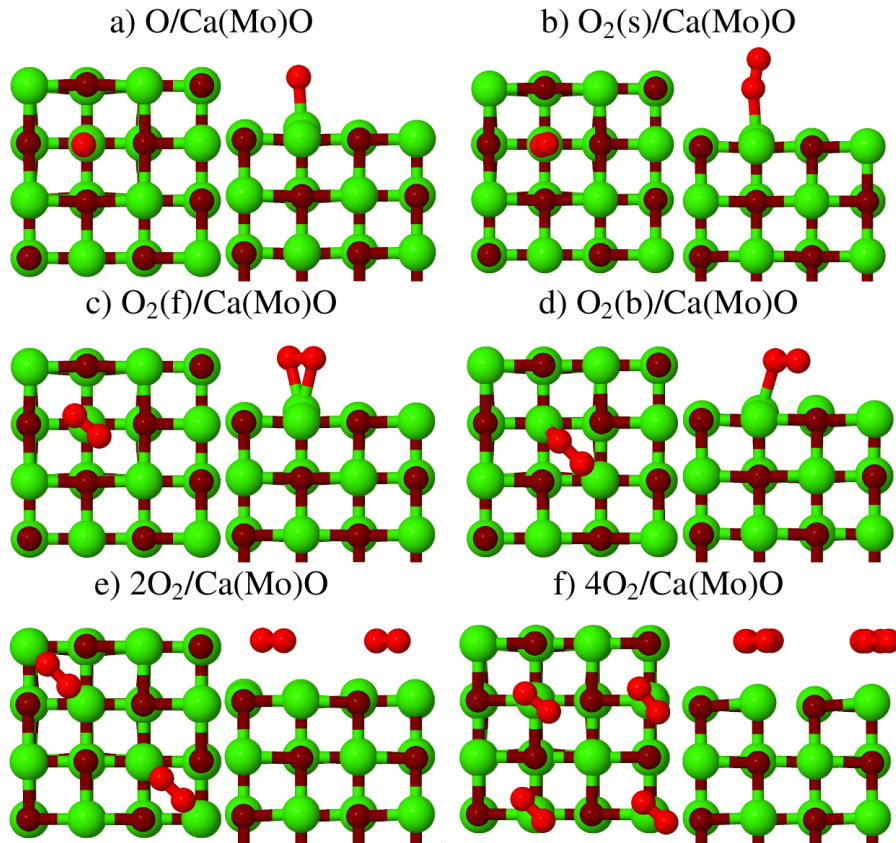
a) O/Ca(Mo)O   b) $O_2(s)$/Ca(Mo)O

c) $O_2(f)$/Ca(Mo)O   d) $O_2(b)$/Ca(Mo)O

e) $2O_2$/Ca(Mo)O   f) $4O_2$/Ca(Mo)O

Figure 3.7: Relaxation geometries for oxygen adsorption on Mo doped CaO(001). The adsorbed oxygens are red, Ca are green, and surface O are brown.

Similar to the Au adatom, the Bader charge analysis and magnetic moments indicate that both the O atom and oxygen molecule are negatively charged on the Ca(Mo)O(001) surface (see Table 3.1). The magnetic moments are close to unity, in-

Table 3.1: Adsorption energies [eV] for O and O_2 divided into the iono-covalent, redox, and Coulomb contributions, the Bader charges [|e|] and magnetic moments [μ_B] for the adsorbed species, the O-O distance [Å] for the adsorbed O_2 and the average distance between Mo and adjacent O^{2-} anions [Å]. The labels s, f, o-a, b note the standing, flat, off-axis and bridge orientations of O_2 respectively. Fig. gives the corresponding sub-figure in Figure 3.7.

Fig.	X	E_{ads}	E_{icov}	E_{redox}	E_{coul}	q_X	μ_X	d_{O-O}	d_{Mo-O}
a)	O	-0.19	2.04	-2.59	0.36	-0.83	0.79		2.25
b)	O_2^s	-1.49	-0.13	-1.61	0.26	-0.65	1.11	1.31	2.28
c)	O_2^f	-1.80	-0.12	-2.00	0.32	-0.80	-0.81	1.35	2.26
	$O_2^{f,o-a}$	-1.80	-0.12	-2.00	0.32	-0.80	0.93	1.35	2.26
d)	O_2^b	-1.92	-0.11	-2.11	0.30	-0.81	0.91	1.34	2.26

dicating that the adsorbed molecules are in a superoxo state. Since the O-O bond length correlates with the charge of the molecule, [55] the charging of O_2 is further supported by the elongated O-O bond lenght that is about 0.1 Å longer on the surface compared with the computational value of 1.23 Å in vacuum. Similarly, the origin of the adsorbates charge can be traced to the dopant by noting that the average distance between Mo and adjacent O^{2-} anions has reduced by 0.04 to 0.07 Å from the value of 2.32 Å for a clean surface. The reduction is due to the change in the formal oxidation state of Mo from 2+ to 3+ since the more positive ion has a shorter ionic radius.

The charge transfer from the dopant to the adsorbate is similar in the adsorption of the Au atom, O atom and O_2 molecule. Therefore, the modified Born-Haber cycle presented in the previous section can also be used to analyze the O and O_2 adsorption analogously to the Au adsorption. The adsorption energies for O and O_2 are split into the iono-covalent, redox, and Coulomb contributions (Table 3.1). Due to the long adsorbate-dopant distance, the increase in surface reactivity due to doping is expected to be caused by the redox mechanism. Indeed, the redox energy is clearly the most dominant term in all the adsorption geometries. Since the effects of adsorbate-dopant distance and the dopant material are not expected to depend on the specific nature of the adsorbate as long as it is an electron acceptor, we did not repeat these analyses for oxygen.

So far all calculations have been done at the GGA level neglecting the known problems of unphysical delocalization of the Mo d-electrons. The description of the d-states can, however, be improved in some cases by including a Hubbard U correction. The adsorption energy and the energy partition was checked against inclusion of a Hubbard U correction to the Mo d-states. For Mo, the U value describing the magnitude of the correction varied from 0 to 9 eV. The adsorption energy as well as the energy partition remained nearly fixed for the U values at or below 3 eV, while the adsorption energy together with the redox energy becomes linearly less exothermic with increasing U

Table 3.2: The average (ave) and differential (dif) adsorption energies [eV] for N O_2 molecules on Ca(Mo)O. The Bader charges [|e|] and magnetic moments [μ_B] for the adsorbed species and the Mo-dopant are also given together with the average O_2 bond length [Å] and the average distance between Mo and adjacent O^{2-} anions [Å].

Fig.1	N	E_{ads}^{ave}	E_{ads}^{dif}	Σq_{O_2}	q_{Mo}	$\Sigma|\mu_{O_2}|$	μ_{Mo}	d_{O-O}	d_{Mo-O}
d)	1	-1.92	-1.92	-0.81	1.63	0.91	2.83	1.34	2.26
e)	2	-1.31	-0.70	-0.97	1.67	2.43	2.71	1.29	2.25
f)	4	-0.70	-0.22	-1.27	1.71	7.69	-3.61	1.28	2.24

when it was set at or above 5 eV. However, only the small values produce the correct spin state predicted by a hybrid functional calculation, which justifies the treatment at the plain GGA level [88].

So far we have considered systems with one to one ratio between the adsorbates and dopants. This ratio depends on two factors, namely the concentration of the dopants and the coverage of adsorbates. Thus, by increasing the oxygen coverage, one can also evaluate the effect of doping concentration, provided that the adsorbate-adsorbate interactions do not become dominant. Since the enhanced binding relies on a redox effect, an increase in the adsorbate coverage hinders the redox mechanism and leads to a less exothermic adsorption, as seen in Table 3.2. The hindering of the redox mechanism is caused by the higher energy cost to extracting more electrons from the dopant, when it has already donated an electron to an adsorbate.

3.2   Gold assisted oxygen dissociation on Mo doped CaO(001)

Dissociation of oxygen is an important reaction step in oxidation reactions. The selective oxidation of hydrocarbons, for example, is an important reaction in the field of catalysis. Unfortunately, using the readily available molecular oxygen from air as a reactant is very problematic. For oxidation to occur, the oxygen molecule needs to be dissociated and the energy required for dissociation is larger than the binding energy of C-H bonds in even the most stable hydrocarbon. This means that introducing enough energy to dissociate oxygen usually leads to complete oxidation of hydrocarbons [89]. Thus, the activation of oxygen is an interesting process from a catalysis perspective. The O_2 molecule is an electronegative species and can easily be charged on oxide thin films [55, 90] or doped oxides with electron rich dopants, as seen in the previous section. Oxygen can also be activated with charge transfer from the edge of a 2D Au cluster [91]. The previous computational study indicates

that the MgO/Ag(001) supported Au_{14} cluster can activate and dissociate multiple oxygen molecules that are adsorbed at the cluster's edge. The oxygen atoms formed in the dissociation are negatively charged and have obtained part of their charge from the Au atoms at the edge of the Au cluster. The Au atoms change their charge state from anionic to cationic, and form linear O-Au-O chains at the edge of the cluster. Ab initio thermodynamical considerations indicate that structures with dissociated oxygen are stable in atmospheric conditions, which suggests that supported Au clusters could potentially be used as catalysts for low temperature oxidation reactions. In this section, a similar analysis is performed for an Au_{19} cluster on Mo doped CaO(001).

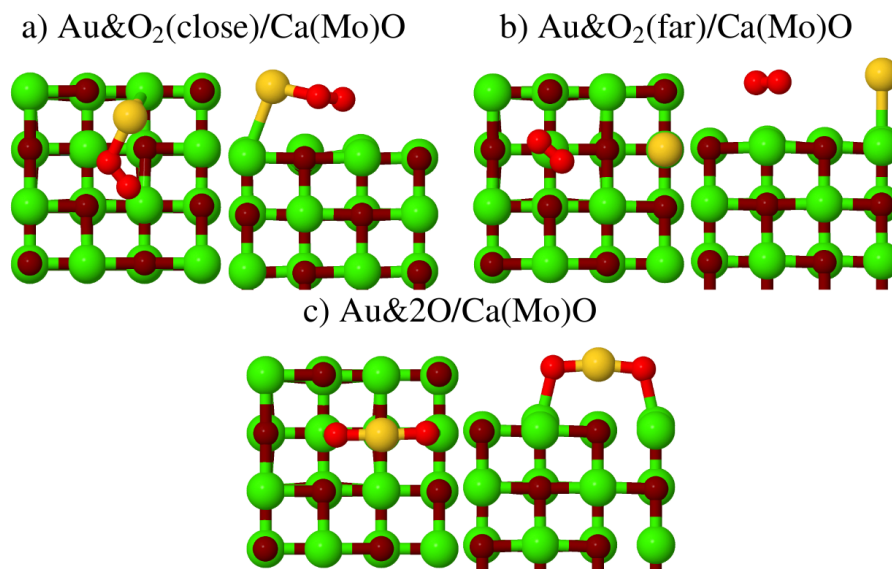### 3.2.1 Oxygen dissociation by a single Au atom on Ca(Mo)O(001)

Figure 3.8: Relaxation geometries for oxygen adsorption on Au/Ca(Mo)O(001). Au is yellow and the rest as in Figure 3.7.

While the molecular adsorption is clearly more exothermic on a clean Mo doped CaO surface, the presence of Au adatoms make the dissociative adsorption energetically favoured. This is seen by considering three adsorption geometries for O_2 on the surface with an Au adatom. Two molecular adsorption geometries, where the O_2 is placed either near the Au adatom on an adjacent bridge site, or further away from Au on a Ca-top site, are contrasted with the third geometry where the molecule is dissociated and the resulting O atoms are on the opposing sides of the Au atom, as shown in Figure 3.8. The corresponding adsorption energies are given at Table 3.3. While the presence of the Au adatom hinders the redox mechanism in the molecular adsorption, the dissociative adsorption is clearly exothermic and the surface with dissociated

Table 3.3: The coadsorption(co), Au, and O_2 adsorption energies [eV] on Ca(Mo)O. The Bader charges [|e|] and magnetic moments [μ_B] for the adsorbed Au and O_2. The minimum distance between the adsorbed species d_{Au-O} is given with the O_2 bond length d_{O-O} and the average distance between Mo and adjacent O^{2-} anions [Å]. The corresponding sub figure in Figure 3.8 is given under Fig. (*: O_2 dissociated)

Fig.	E_{co}	E_{Au}	E_{O_2}	q_{Au}/q_{O_2}	μ_{Au}/μ_{O_2}	d_{Au-O}	d_{O-O}	d_{Mo-O}
a)	-3.27	-1.36	-0.57	-0.18/-0.73	0.0/-0.1	2.17	1.34	2.25
b)	-2.91	-1.11	-0.20	-0.61/-0.34	0.0/-1.1	4.39	1.28	2.25
c)	-4.33	-2.54	-1.63	0.53/-1.57	0.6/1.2	1.90	3.79*	2.24

molecule is over 1 eV more stable than the most stable geometry with an intact molecule. This is due to a change in the charge state of the Au adatom from anionic to cationic, which resolves the competition for the dopant charge between Au and oxygen.

For all geometries shown in Figure 3.8, the adsorbate species have obtained one electron from the Mo dopant. This is seen from the Bader charges of the adsorbed species and the negligible changes in the Mo-O_2^{2-} distance. The Bader charges for the adsorbates always add up to approximately negative one and the nearest neighbour distance indicates that the ionic radius of Mo stays fixed showing that the oxidation state of Mo remains unchanged. However, the charge states of the adsorbates differ between the geometries. When Au and O_2 have long separation over 4 Å, the Bader charges of both species are clearly more neutral than when they are in separate computational cells. The Bader charges of the Au atom and O_2 molecule are -0.8 |e| and -0.9 |e| in separate computational cells, while they are -0.6 |e| and -0.3 |e| in the same computational cell, respectively. The decrease in charge reflects the competition for the available dopant electron, with the Au atom being slightly more negative, possibly due to its higher electron affinity compared with the molecule. If the adsorbates are closer together, with about 2.2 Å Au-O_2 distance, they no longer have clearly defined individual states, but their states become hybridized as seen from PDOS analysis (not shown). The O_2 atoms have a magnetic moment of nearly zero that reflects the hybridization with Au adatom. In this geometry, the charge competition is in a sense solved by the delocalization of the dopant electron over both species. Finally, in the geometry with the dissociated molecule, the O atoms have a combined Bader charge of -1.6 |e| and the Au atom appears cationic with a Bader charge of 0.5 |e|, indicating the formation of Au^{1+} oxide. In this case, the charge competition is solved by a change in the charge transfer characteristic of Au, since instead of obtaining charge, the Au adatom acts now as a charge donor.
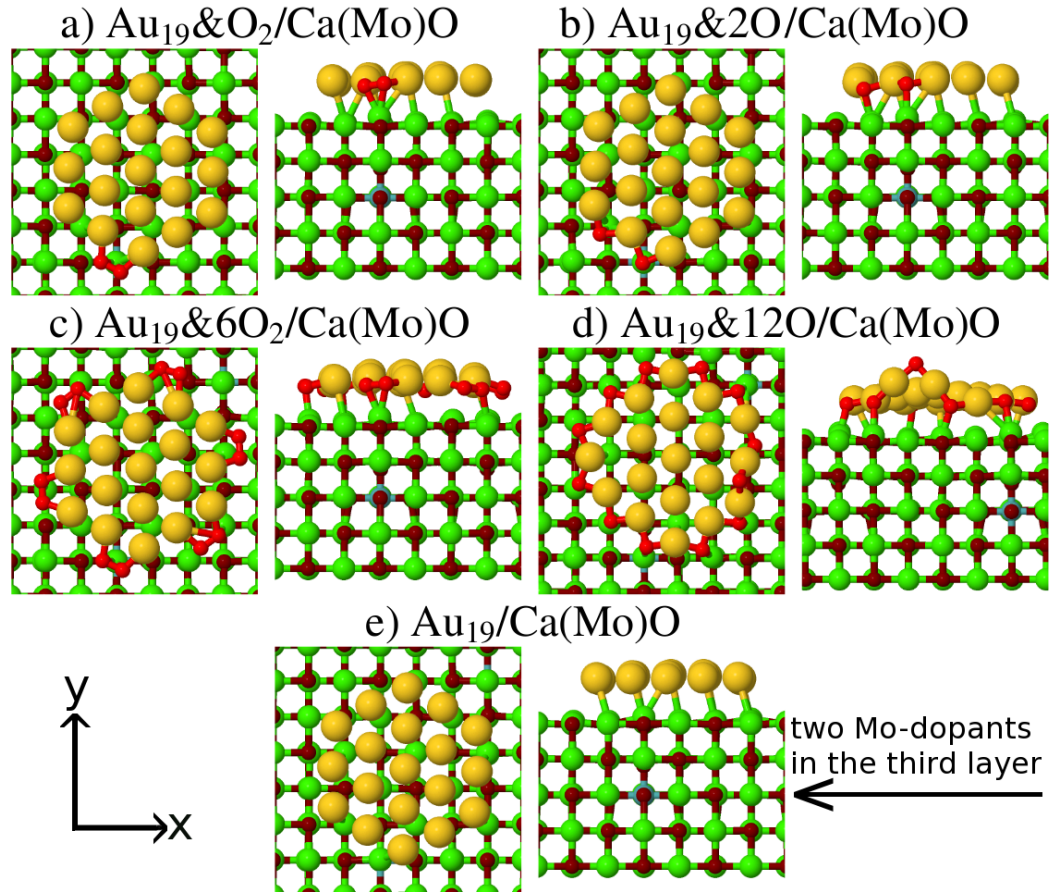
3.2.2   Oxygen dissociation on Au_{19}/Ca(Mo)O(001)

Figure 3.9: Relaxation geometries for oxygen adsorption on the edge of Au_{19} cluster on Ca(Mo)O(001). Mo is blue and the rest as in Figure 3.8.

In the previous section, the ability of a single anionic Au atom to dissociate oxygen on a Ca(Mo)O support was discussed. However, in all but the most precisely controlled low temperature conditions, the sintering of Au atoms is possible and Au grows into clusters. Therefore, the interaction between oxygen and Au clusters is considered in this section. The Au_{19} cluster is chosen as a model system, since it exhibits hexagonal symmetry and is roughly in the size scale of the experiments. The Au cluster is placed on a five-layer thick CaO slab that has two Mo dopants in the 3rd layer in non adjacent positions. Adsorption geometries with intact and dissociated molecules are considered in order to address the oxygen activation and dissociation. It is known from previous computational work that oxygen adsorption is endothermic on the interior of a 2D Au_{14} cluster and hence, the adsorption is considered only at the cluster edges [91]. The effect of oxygen coverage is addressed by studying the adsorption and dissociation of a single molecule as a low coverage case and the adsorption of six oxygen molecules

as the high coverage regime. Figure 3.9 shows the considered adsorption geometries with the pristine Au_{19} cluster.

The molecular adsorption of a single O_2 molecule is exothermic with an adsorption energy close to -1 eV. Again, as with one Au adatom, the dissociative adsorption is energetically preffered by almost 1 eV, as seen in Table 3.4. The charge transfer to oxygen also resembles the single Au adatom case with the intact molecule having a Bader charge of -1.1 |e|, while the dissociated oxygen has a more negative total charge of -1.8 |e| compared with the intact molecule. The charging behaviour of Au is also similar to the single Au atom case, since a Bader charge analysis indicates the appearance of cationic Au between the O atoms resulting from the dissociation, see Figure 3.10. The dissociation barrier to a single molecule is 0.6 eV, which is relatively low and only 0.1 eV higher than the barrier at the edge of Au_{14} cluster on MgO/Ag(001) [91].

Table 3.4: The average adsorption energies for O_2 on Au_{19}/Ca(Mo)O-surface. The total Bader charges [|e|] for adsorbates and the average for the Mo dopants. The average magnetic moments [μ_B] for the Mo-dopants. The magnetic moments for adsorbates are zero in all cases. The average O_2 bond length [Å].

Fig.	X	$E_{ads}^{ave}(O_2)$	Σq_{O_2}	$q_{Au_{19}}$	q_{Mo}	μ_{Mo}	d_{O-O}
a)	O_2	-1.04	-1.09	-3.01	2.00	-1.50	1.49
b)	2O	-1.93	-1.82	-2.51	2.06	-1.38	
c)	$6O_2$	-0.92	-6.07	0.54	2.13	-0.84	1.47
d)	12O	-1.51	-10.28	4.24	2.19	0.00	
e)				-3.96	2.05	1.55	

Increasing the oxygen coverage does not change the main results from the low coverage case. While the dissociative adsorption becomes slightly less exothermic on average for six molecules, it remains clearly favored over the molecular adsorption. All the adsorbed molecules have Bader charges close to one, as do the O atoms in the dissociated geometries. The charge originates from the Mo dopants and from the Au atoms at the edge of the cluster, that change from cationic to anionic. In this model, all the Mo valence electrons from both dopants can be donated to adsorbates as seen from their zero magnetic moments in the geometry with six dissociated molecules. The Bader charges of the adsorbates also support the full oxidation of the dopants. Eight of the 12 electrons obtained by the O atoms originate from the dopants, and four from the Au cluster that has a Bader charge of 4.24 |e|. Note that two of the valence electrons of each Mo dopant are donated to the oxide. The formation of dopants with formal oxidation state 6+ may be kinetically hindered in the more realistic systems but the higher oxidation states are not required for higher dopant concentrations. The full oxidation of the Au cluster edge can be achieved by having more dopants with a lower oxidation state.
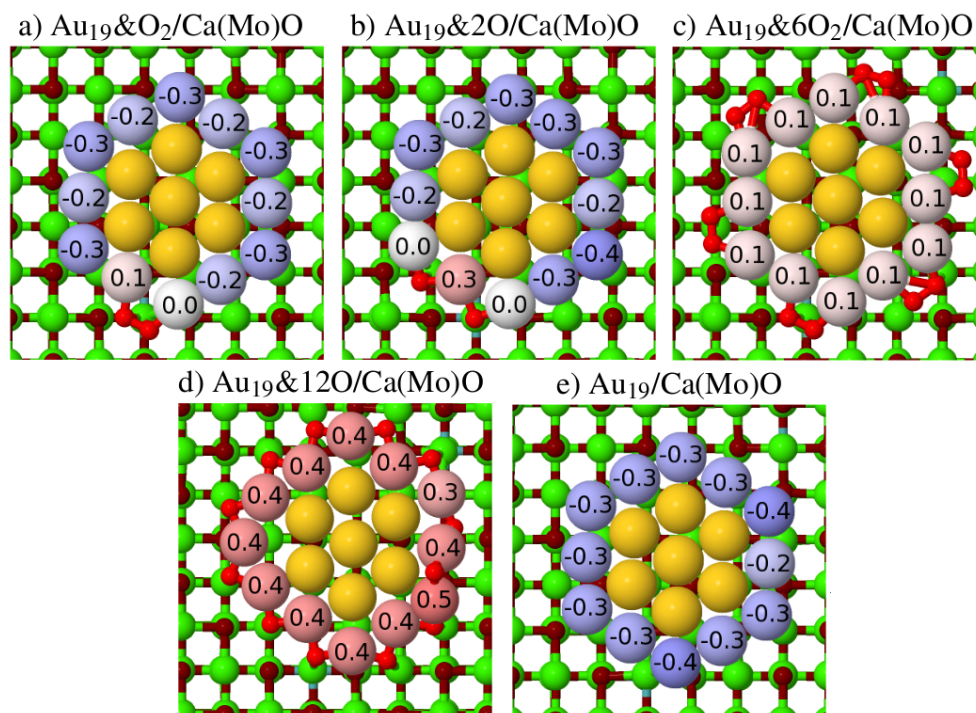
Figure 3.10: The Bader charges of the edge Au atoms of the Au_{19} cluster on Ca(Mo)O(001) with different amounts of adsorbed oxygen. The edge Au atoms are blue when negative and the rest of the colors as in Figure 3.9.

The oxidation of the cluster edges changes the shape of the Au_{19} cluster from hexagonal into more square-like. The 120-degree angles at the edges of the hexagonal cluster do not facilitate the formation of linear O-Au-O chains as well as the straight angles of a square. The more square-like shape of the cluster can be quantified by considering the ratio of the circumference of the cluster to the diameter of the cluster. The circumference C can be defined as the sum of the distances between the nearest neighbour edge atoms and the diameter D as the longest distance between two edge Au atoms. The ratio C/D is 3.00 for the pristine Au_{19} cluster without the O atoms while it is 2.95 for the cluster with fully oxidized edge. The ratio is 3 for ideal hexagon and $2\sqrt{2} \approx 2.83$ for a square.

3.3 Water on Au/MgO/Ag(001)

Many oxide surfaces are hydroxylated in ambient conditions, [92] which can change their chemical properties [93–96] and their atomic structure. For example, cubic MgO(001) crystals can transform to octahedral MgO(111) when in contact with wa-

ter [97]. Interestingly, though water interacts weakly with bulk MgO terraces, [98] it is known to dissociate spontaneously on stepped MgO thin films dupported by Ag(001) [8]. This is a very important reaction step, i.e.- water splitting, where one or two hydrogen atoms are dissociated from a water molecule, in the water-gas shift reaction. The energetics of water adsorption on MgO/Ag(001) terraces depends greatly on the film thickness, since dissociative adsorption becomes exothermic for a monolayer thick MgO, while it remains endothermic on thicker films with a gas-phase molecule as a reference [99]. Computations show that the introduction of Au on MgO/Ag(001) surface gives rise to an attractive electrostatic interaction between the polar water molecule and negatively charged edge of an Au_8 cluster stabilizing the molecule [100].
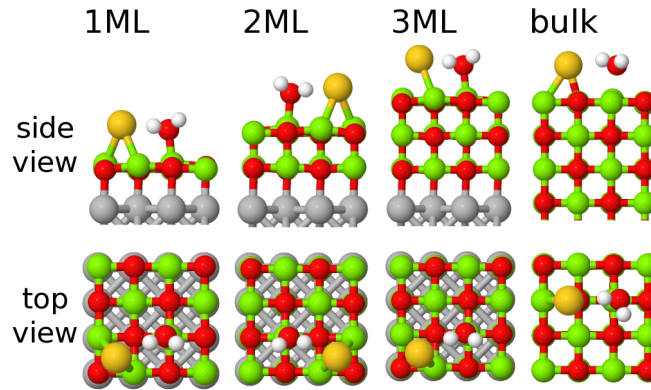
3.3.1   Molecular adsorption

Figure 3.11: Relaxation geometries for the molecular adsorption of water on Au/MgO/Ag(001) surfaces with varying film thickness. Ag is grey, Au is yellow, H is white, Mg is green, and O is red.

To study the coadsorption of water and Au, we placed the water molecule and Au-adatom on adjacent sites with water on the Mg-top site and Au on either a hollow or O-top site on thin film and bulk surfaces, respectively. One H-O bond in the molecule orients towards the adsorbed Au atom for all film thicknesses, with a Au-H distance of about 2.2 Å. The orientation of the second H-O bond is more parallel to the surface on the thin films compared with the more perpendicular orientation on bulk MgO. The adsorption geometries are shown Figure 3.11. The adsorption energy for water is 0.9 eV on the thin films, while it is 0.4 eV on the Au/MgO(001). The added stability on the thin film surface correlates with the charge state of the Au atom. While the Au atom is neutral on the bulk MgO(001) with a Bader charge 0.3 |e| and a magnetic moment of 0.5 μ_B, it is anionic on thin films with a Bader charge close to −0.8 |e| and a zero magnetic moment. Thus, the more stable water molecule on thin films is the result of an attractive electrostatic interaction between the anionic Au atom and the polar H-O bond.
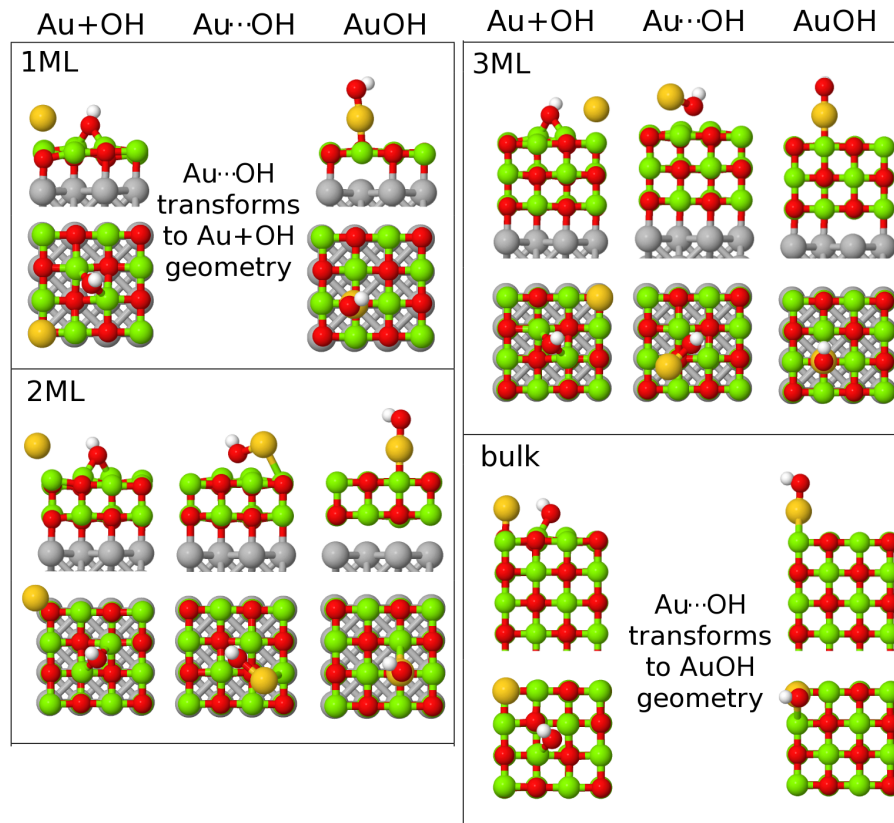
3.3.2 OH adsorption

Figure 3.12: Relaxation geometries for OH adsorption on Au/MgO/Ag(001) surfaces with varying film thickness. Colors as in Figure 3.11.

In order to study dissociative water adsorption, the adsorption properties of the dissociation products H and OH are studied in separate computational cells first. The OH adsorption is considered on three adsorption sites differing in their Au-OH distances for all four film thicknesses. The OH group is either placed on a bridge site between Mg cations with a long Au-OH distance (Au+OH), on the surface adjacent to the Au adatom (Au$\cdots$OH), or directly on top of the Au adatom (AuOH). The adsorption geometries are displayed in Figure 3.12. Note that for a ML thick film (bulk MgO) the Au$\cdots$OH initial geometry transforms to Au-OH (AuOH) geometry without an energy minimum in-between. In the AuOH geometry, the Au-O distance is about 2 Å and the Au atom is on an O-top site on all the surfaces.

The OH adsorption energies are shown in Figure 3.13. Interestingly, the adsorption energies in the Au+OH and AuOH geometries have the opposite dependence on film thickness. While the OH adsorption energy becomes more exothermic with increasing film thickness, when the adsorbates are far apart, the trend is reversed when OH is
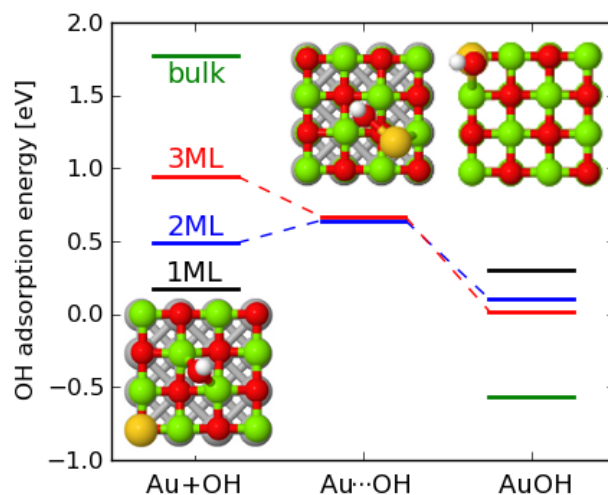
Figure 3.13: Adsorption energies for OH on Au/MgO/Ag(001) with varying film thickness. The insert shows the surface where the OH adsorbate is the most stable. Colors as in Figure 3.11.

adsorbed on top of Au adatom. This correlates with the direction of charge transfer in these two geometries. Charge is transfered from the metal-oxide interface to the OH group the in Au+OH geometry, while charge is transferred to the interface in the AuOH geometry. This is seen from the Bader charges of Au and OH. While both Au and OH exhibit negative charging on thin films, the AuOH species is neutral.

3.3.3   H adsorption

Next the adsorption of H is discussed. Similar to the OH adsorption, three different adsorption sites are considered on all four surfaces. The studied geometries for H adsorption are on an O-top site far away from the Au adatom, on the oxide adjacent to the Au atom, and directly on top of the Au atom noted Au+H, Au···H and AuH, respectively. The adsorption geometries are shown in Figure 3.14. Note again the formation of AuH species with Au-H distance of 1.6 Å for all surfaces.

The adsorption energies are given in Figure 3.15. In this case, the adsorption on bulk MgO is the most exothermic for each of the considered geometries. Further, there is a trend reversal for the thin film MgO/Ag(001) surfaces between the Au+H and AuH geometries. While the adsorption in the Au+H geometry becomes more exothermic with decreasing film thickness, the opposite holds on the AuH geometry. Still, the adsorption on bulk MgO(001) is the most exothermic in both geometries. Similarly as in the OH adsorption case, the reversed energy dependence on the film thickness correlates with the direction of charge transfer. The formed AuH species is neutral, the charge transfers from the Au to the interface. The stabilization due to the charging
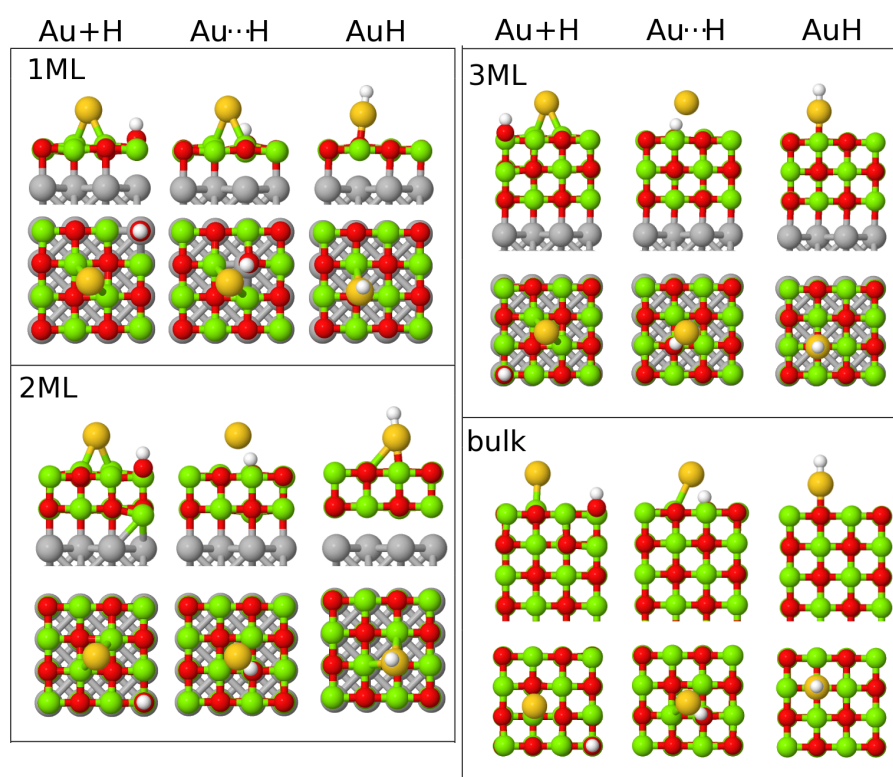
Figure 3.14: Relaxation geometries for H adsorption on Au/MgO/Ag(001) surfaces with varying film thickness. Colors as in Figure 3.11.
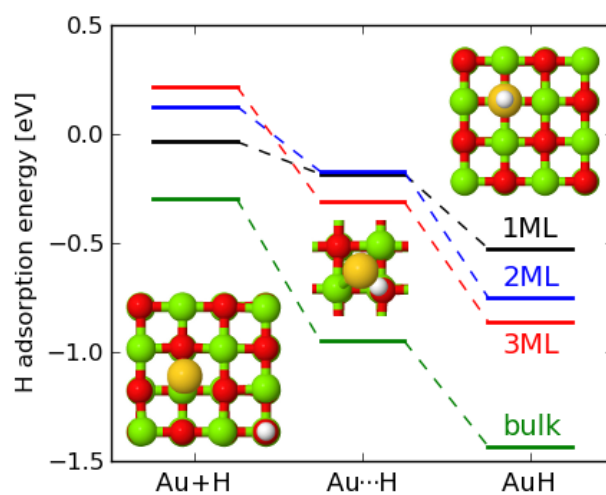

Figure 3.15: Adsorption energies for H on Au/MgO/Ag(001) with varying film thickness. The insert shows the surface where the H adsorbate is the most stable. Colors as in Figure 3.11.

of Au is more exothermic for thinner films and the loss of this energy makes the H adsorption on thicker films more exothermic. In H adsorption on the oxide surface, the O^{2-} anion is transformed to a surface OH^- group, and the resulting electron is transferred to the interface on MgO/Ag(001) or the Au adatom on bulk MgO(001). Since Au has high electron affinity, the H adsorption on bulk becomes favored over the adsorption on thin films where the Au adatom is already anionic.
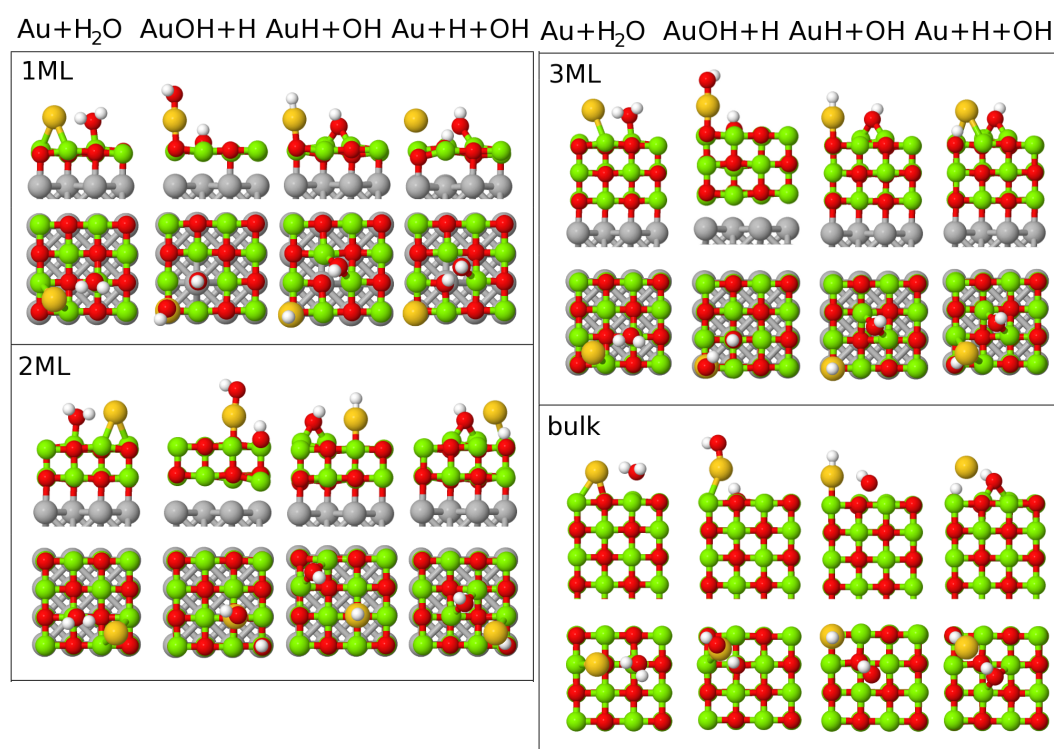
3.3.4 Dissociative adsorption

Figure 3.16: Relaxation geometries for water adsorption on Au/MgO/Ag(001) surfaces with varying film thickness. Colors as in Figure 3.11.

Here, we focused on three geometries that are differentiated by the product for the dissociative adsorption. These are AuOH+H, AuH+OH, and Au+H+OH as shown in Figure 3.16. There are multiple possible configurations and, as mentioned above, the ones focused on here are differentiated by the dissociation product, if any, that is adsorbed on top of Au. This is done to study the effect of Au on the dissociation. Also, in more realistic systems, the diffusion barriers are low and at modest temperatures, different oxide configurations can transform into other morphologies. Therefore, the search for the absolute minimum geometry is not important for conclusions on the effect of Au.
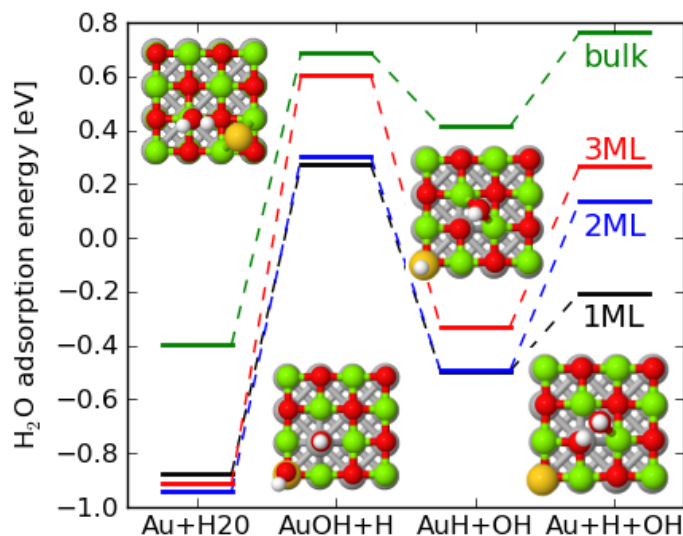
Figure 3.17: Adsorption energies for water molecule on Au/MgO/Ag(001) with varying film thickness. The insert shows the surface where the molecular or dissociated water molecule is the most stable. Colors as in Figure 3.11.

The most stable geometry with dissociated water is AuH+OH for all film thicknesses as seen in Figure 3.17. The reason for this is two fold. Firstly, the H adsorption energy on the Au top site was the most exothermic adsorption site for H without the OH group. Secondly, the charge transfer does not increase the basicity of the surface, contrary to the geometry with AuOH species. If H adsorbs on Au top site, the electron from anionic Au is available to the OH group and does not require charge transfer with the surface. If OH adsorbs on Au top site however, the electron from both Au and formed surface OH group is transfered to the interface making the adsorption less exothermic. In a sense, the formation of AuOH increases the basicity of the surface and weakens the subsequent H adsorption, while the formation of AuH increases the basicity of the surface, this time making the adsorption of OH more exothermic.

3.3.5   Scaling between H and OH adsorption

In the previous sections, it was noted that the adsorption energies for both H and OH on the Au/MgO/Ag(001) surface are more exothermic with increasing film thickness, which is contrary to the usual trend of less exothermic adsorption with increasing film thickness. This trend reversal was connected to charge transfer from Au adatom due to the formation of neutral AuH and AuOH species. The formation of neutral adsorbate species also gives a scaling relation between the adsorption energies of H and OH shown in Figure 3.18.
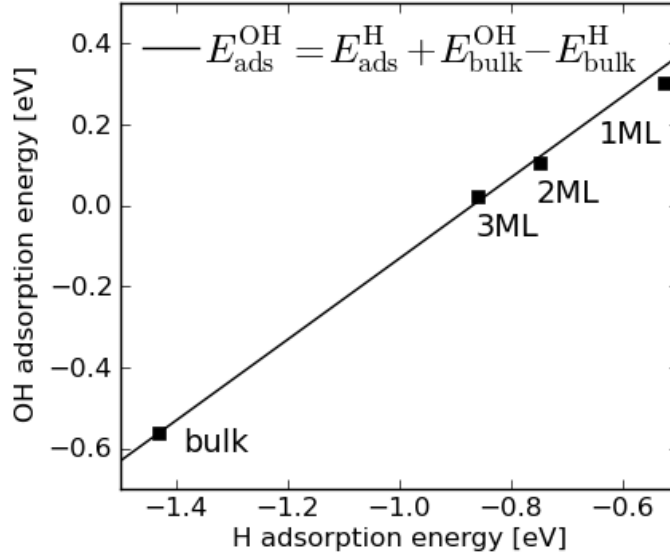
Figure 3.18: Scaling between H and OH adsorption energies on the Au/MgO/Ag(001) surface.

To explain this, let us consider the adsorption of H in two steps. First, anionic Au changes to neutral via charge transfer to the MgO-Ag interface

$$\mathrm{Au^-/MgO/Ag(001)^+ \rightarrow Au/MgO/Ag(001)}. \tag{3.2}$$

The energy associated with this process $-E_{CT}(n)$ depends on the film thickness n becoming less exothermic for thicker films, but does not depend on the adsorbate. Second, the formation of covalently bonded AuH species on the surface occurs,

$$\mathrm{H(g) + Au/MgO/Ag(001) \rightarrow AuH/MgO/Ag(001)}. \tag{3.3}$$

The energy associated with this process depends mainly on the local interaction between Au and H, and can be approximated to be independent of the film thickness. By combining the previous reactions, the adsorption energy for H can be written as

$$E_{\mathrm{ads}}^{\mathrm{H}}(n) = E_{\mathrm{bulk}}^{\mathrm{H}} - E_{CT}(n) \tag{3.4}$$

where $E_{\mathrm{bulk}}^{\mathrm{H}}$ is the H adsorption on the bulk Au/MgO(001) surface. Note that by the same reasoning, the OH adsorption energy is

$$E_{\mathrm{ads}}^{\mathrm{OH}}(n) = E_{\mathrm{bulk}}^{\mathrm{OH}} - E_{CT}(n) \tag{3.5}$$

where E_{bulk}^{OH} is the OH adsorption on the bulk Au/MgO(001) surface. By eliminating E_{CT} from equation (3.5) by using equation (3.4), one gets the scaling relation between H and OH adsorption energies. Since E_{CT} does not depend on the adsorbate X and as long as the AuX end product is neutral, this scaling should generalize to other suitable adsorbates as well.

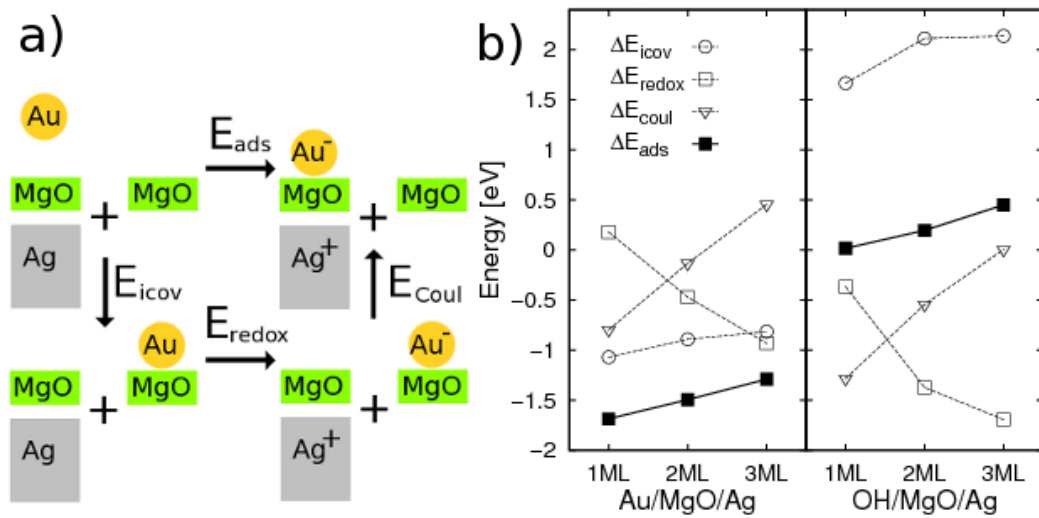### 3.3.6 Born-Haber cycle for MgO/Ag(001) thin film surface

Figure 3.19: **a)**A schematic representation of the modified Born-Haber cycle for a thin film surface. **b)** The calculated energy contributions for Au and OH adsorption on MgO/Ag(001) with one, two and three ML thick MgO film.

The Born-Haber approach has thus far been used for the doped oxides, but it can be generalized to the thin film arrangement. This is shown schematically in Figure 3.19**a)**. The adsorption of Au and OH is considered on Ag(001) supported MgO films that range from one to three layers in thickness and the results are shown in Figure 3.19**b)**. The electrostatic stabilization of the adsorbate given by the Coulomb term is an important energy contribution for the ML thick film. However, the adsorption remains more exothermic compared with the pristine oxide also for the thicker films, where Coulomb contribution is small. It turns out that while the Coulomb energy displays the $1/r$ behaviour, the redox energy compensates for the lost electrostatic stabilization. The surface work function is smaller for the 2ML thick film compared with the 1ML thick film, making the removal of an electron energetically easier for the thicker film and thus, the redox energy more exothermic.

Interestingly, the energies describing the Coulomb interaction do not approach zero when the distance between negative adsorbate and positive support becomes large.

This is contrary to the expected behaviour between charges with opposite signs. This effect is explained by the structural relaxations and the definition of E_{Coul}. The oxide lattice is highly ionic and its structure changes in the presence of charges. In particular, the cations move towards negatively charged adsorbates while the anions move away from them. Consider a simple model for the energetics of these distortions where the oxide ions are confined by a harmonic potential. The energy associated with the deformation of the oxide film is given by

$$E = \sum_i \frac{1}{2} k \boldsymbol{x}_i^2 \tag{3.6}$$

where k is an elastic constant related to the properties of the oxide and $\boldsymbol{x}$ is the displacement of ion i due to charged adsorbates and support. The displacements are due to the electrostatic forces caused by the electric fields of the charged adsorbates $\boldsymbol{E}_a$ and the support $\boldsymbol{E}_s$. The displacements in the presence of an electric field $\boldsymbol{E}$ are

$$\boldsymbol{x}_i = \frac{q_i}{k} \boldsymbol{E}(\boldsymbol{R}_i) \tag{3.7}$$

where q_i and $\boldsymbol{R}_i$ are the charge and position of ion i. Using this model, the energy difference associated with the distortion of the oxide in the redox step is

$$\Delta E = \sum_i \frac{1}{2} q_i^2 (\boldsymbol{E}_a(\boldsymbol{R}_i) + \boldsymbol{E}_s(\boldsymbol{R}_i))^2 - \sum_i \frac{1}{2} q_i^2 \boldsymbol{E}_a(\boldsymbol{R}_i)^2 - \sum_i \frac{1}{2} q_i^2 \boldsymbol{E}_s(\boldsymbol{R}_i)^2 \tag{3.8}$$

where the first term on the r.h.s. is the energy of a system with both charged adsorbate and charged support, while the second and third term are the energies for systems with only charged adsorbate and charged support. The equation simplifies into

$$\Delta E = \sum_i q_i^2 \boldsymbol{E}_a(\boldsymbol{R}_i) \cdot \boldsymbol{E}_s(\boldsymbol{R}_i). \tag{3.9}$$

Note that due to symmetry the $\boldsymbol{E}_s$ is parallel to the surface normal in the z-direction. This entails that $\boldsymbol{E}_a(\boldsymbol{R}_i) \cdot \boldsymbol{E}_s(\boldsymbol{R}_i) = E_a^z(\boldsymbol{R}_i) E_s(\boldsymbol{R}_i)$ where $E_a^z(\boldsymbol{R}_i)$ and $E_s(\boldsymbol{R}_i)$ are the z components of the electric fields of the adsorbate and support, respectively. Since the z components of the electric fields are in the same direction in the oxide, $\boldsymbol{E}_a(\boldsymbol{R}_i) \cdot \boldsymbol{E}_s(\boldsymbol{R}_i) > 0$ and therefore $\Delta E > 0$, which gives a positive contribution to the redox energy. Similar reasoning explains the positive Coulomb contribution in cases of thick doped oxides because most of the displacements of the oxide ions occur between the adsorbate and dopant.

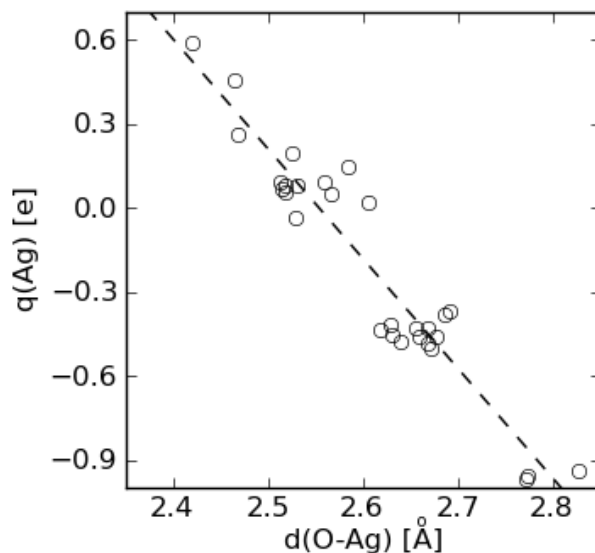## 3.4   Charge-structure correlations in modified oxides

Figure 3.20: The linear correlation between MgO-Ag interface distance and total Ag charge.

As seen in the previous section, the charged adsorbates cause distortions in the highly ionic oxide ions. These distortions can be used to estimate the charge states of different parts of the systems, such as adsorbates and dopants utilizing correlations between charges and structures. Since the atomic structures are defined by the coordinates of the atoms, the evaluation of charges using these is much simpler than using the electronic density. The atomic structures are known to correlate with charge states of the atoms. For example, the bond length in the O_2 molecule correlates linearly with the Bader charge of the molecule [55]. In this thesis, I report three correlations between Bader charges and atomic structures. The first correlation is between the interface distance and the interface charge. The interface distance is defined for the MgO/Ag(001) thin film arrangement as the difference between the average z-coordinate of the O anions in the lowest MgO layer and the average z-coordinate of the Ag atoms in the highest Ag layer. The interface charge is the charge associated with the MgO-Ag interface and it can be interpreted as the Bader charge of the Ag atoms. These correlate linearly as shown in 3.20.

This correlation is similar to the correlation between O_2 charge and bond length. It can be rationalized as follows: when the level alignment between adsorbate states and the interface states favours the charging of the interface, the interface stretching becomes energetically favorable to accommodate the extra charge. The next correlation is between the rumpling of the MgO film and the charge difference over the film. The rumpling of the oxide describes the polar distortion of the strongly ionic MgO and
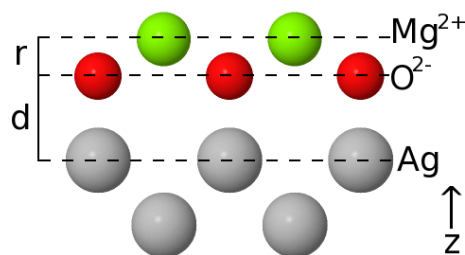
Figure 3.21: A schematic representation of the oxide rumpling r and the MgO-Ag interface distance d.
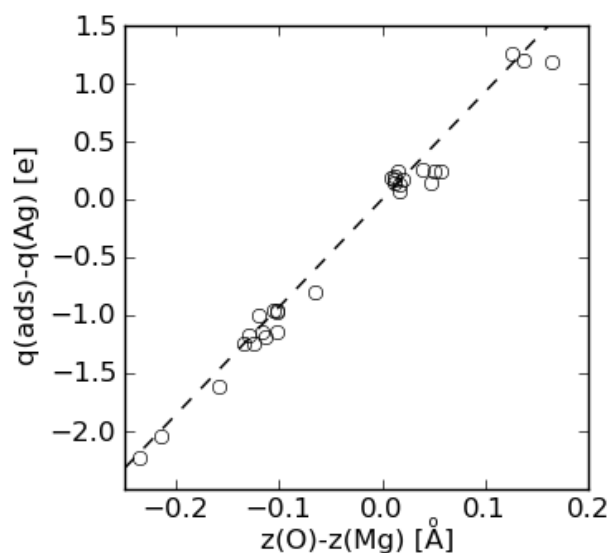

Figure 3.22: The linear correlation between charge difference over the MgO film with the rumpling of the film.

it can be defined as the difference between the average z-coordinate of the anions and cations in the film. In 3.21 the rumpling of a MgO film is shown schematically. The charge difference over a MgO film is defined as the total charge of Ag atoms subtracted from the total charge of adsorbates. The adsorbates are on top of the film and a positive adsorbate induces an upward force towards the negative anions in the film. Contrarily, the Ag atoms are underneath the film and positive Ag atoms exerts a downward force to the negative anions in the film. Thus it is not surprising that the amount of rumpling correlates with the charge difference between adsorbates and Ag support. This linear correlation is shown in 3.22. Lastly, the rumpling of a Mo doped CaO correlates with the adsorbate-dopant distance when an Au atom has adsorbed on the surface. This correlation is shown in 3.23. In this section, a simple model is presented to rationalize the correlations with rumpling.
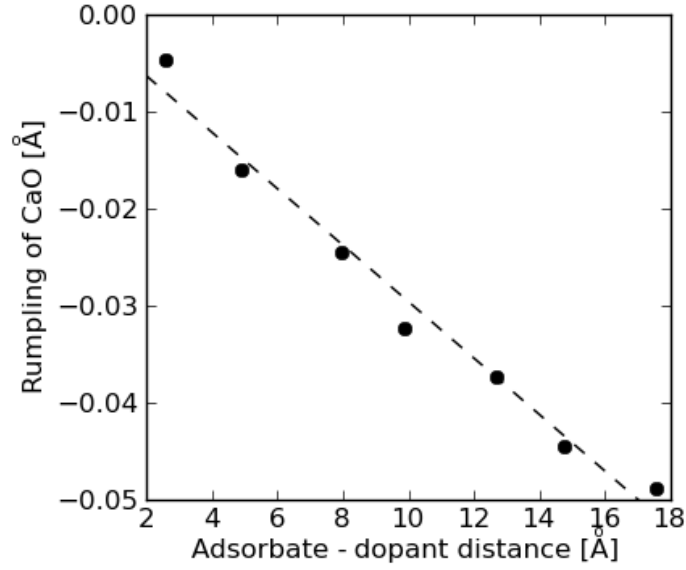
Figure 3.23: The linear correlation between adsorbate-dopant distance and the rumpling of the film.

The correlations hold for equilibrium systems where it is a reasonable assumption that the center of positive charge is close to the center of negative charge, which is given by the charge distribution $n(\boldsymbol{r})$

$$\int \mathrm{d}\boldsymbol{r} n(\boldsymbol{r})\boldsymbol{r} = \sum_a Z_a \boldsymbol{R}_a \tag{3.10}$$

where Z_a and $\boldsymbol{R}_a$ are the proton number and the position vector of atom a, respectively. Note that the integration is over the whole system. To get a simplified connection between the atomic structure given by the coordinates $\boldsymbol{R}_a$ and the Bader charges of atoms, we take a simple approximation for the electron density

$$n(\boldsymbol{r}) \approx \sum_a Q_a \delta(\boldsymbol{r} - \boldsymbol{R}_a) \tag{3.11}$$

where Q_a is the total negative charge assigned to atom a by the Bader method. Essentially, the approximation is that the negative charge is maximally localized to the atomic nuclei. Substituting this into eqation (3.10) gives the algebraic equations

$$\sum_a q_a \boldsymbol{R}_a \approx 0 \tag{3.12}$$

where $q_a = Z_a - Q_a$ is the charge difference of atom a when compared with a neutral atom.

The equation (3.12) is quite general, since we have not yet specified the specific system under consideration. Let us first consider the MgO/Ag(001) thin film arrangement. Since the surface is periodic in the xy-plane, the equation of interest is the equation for the z-coordinates of the atoms. Denoting the z-coordinate of atom a with z_a, the sum in this case can be split into four different parts

$$\sum_{a \in \text{ads}} q_a z_a + \sum_{a \in \text{Ag}} q_a z_a + \sum_{a \in \text{Mg}} q_a z_a + \sum_{a \in \text{O}} q_a z_a \approx 0. \tag{3.13}$$

where the sum over ads is the sum over all adsorbate atoms, the sum over Ag is over all Ag atoms, the sum over Mg is the sum over all Mg atoms in the film, and the sum over O is the sum over all O atoms in the film. Since the adsorbates are all on the surface, their z-coordinates are approximately equal

$$z_a \approx z_{\text{ads}} \ \forall a \in \text{ads}. \tag{3.14}$$

Further, since Ag atoms below the topmost layer are nearly neutral, i.e. $q_a \approx 0$ for Ag atoms not in the top layer, and the atoms in the same layer have nearly the same z-coordinates, a similar equation can be written for Ag

$$z_a \approx z_{\text{Ag}} \ \forall a \in \text{Ag}. \tag{3.15}$$

With these approximations, the first sums in equation (3.13) can be written as

$$\sum_{a \in \text{ads}} q_a z_a + \sum_{a \in \text{Ag}} q_a z_a \approx q_{\text{ads}} z_{\text{ads}} + q_{\text{Ag}} z_{\text{Ag}} \tag{3.16}$$

where q_{ads} and q_{Ag} are the combined charges of adsorbate atoms and Ag atoms, respectively. Further, since the zero point for z-coordinate can be chosen arbitrarily, it can be chosen such that $z_{\text{ads}} = -z_{\text{Ag}} := w/2$. Note that with this coordinate choice the w corresponds to the distance between the Ag top layer and average adsorbate height or roughly the film thickness. This can further be written as the number of MgO layers n times half of the MgO lattice constant a, i.e. $w \approx na/2$. Using these approximations, the first two sums in equation (3.13) are

$$\sum_{a \in \text{ads}} q_a z_a + \sum_{a \in \text{Ag}} q_a z_a \approx \frac{na}{4}(q_{\text{ads}} - q_{\text{Ag}}). \tag{3.17}$$

The anions and cations in the oxide have approximately equal but opposite charges, i.e. if the charge for Mg cations is q, then the charge of O anions is $-q$. This means that two last sums in equation (3.13) can be combined

$$\sum_{a \in \text{Mg}} q_a z_a + \sum_{a \in \text{O}} q_a z_a \approx q \left(\sum_{a \in \text{Mg}} z_a - \sum_{a \in \text{O}} z_a \right). \tag{3.18}$$

Further, note that the rumpling of the MgO film is given by

$$r = \frac{1}{N} \left(\sum_{a \in \text{O}} z_a - \sum_{a \in \text{Mg}} z_a \right) \tag{3.19}$$

where N is the number of anions or cations in the MgO film. Further, the total number O or Mg ions in the film is given by $N = n N_{ML}$ where N_{ML} is the number of anions in a single MgO layer. Combining equations (3.17) and (3.18) with (3.13) gives the linear relation

$$q_{\text{ads}} - q_{\text{Ag}} \approx \frac{4 N_{ML} q}{a} r \tag{3.20}$$

corresponding to the correlation shown in figure 3.22. Note that the thickness of the film does not affect the relation between rumpling and charge difference. Similarly, beginning from equation (3.12) the correlation for the doped oxide can be explained. Again the sum can be split into

$$\sum_{a \in \text{Ca}} q z_a - \sum_{a \in \text{O}} q z_a + q_{\text{Cr}} z_{\text{Cr}} + q_{\text{Au}} z_{\text{Au}} \approx 0. \tag{3.21}$$

where the sums are over all cations and anions. The charge transfer is from the dopant to the adsorbate

$$q_{\text{Cr}} = q - q_{\text{Au}}. \tag{3.22}$$

This gives the linear relation

$$r_{\mathrm{Cr}} = \frac{q_{\mathrm{Au}}}{Nq} d_{\mathrm{Au-Cr}} \qquad\qquad (3.23)$$

where the rumpling r_{Cr} is defined by the equation

$$N r_{\mathrm{Cr}} = \sum_{a \in \mathrm{O}} z_a - \sum_{a \in \mathrm{Ca}} z_a - z_{\mathrm{Cr}}, \qquad\qquad (3.24)$$

the adsorbate-dopant distance as $d_{\mathrm{Au-Mo}} = z_{\mathrm{Au}} - z_{\mathrm{Cr}}$, and N is the number of O anions.

3.5   Isophorone on Au/MgO/Ag(001)

Isophorone is an α, β-unsaturated cyclic ketone with the chemical formula $C_9H_{14}O$. It has two double bonds and can be used as a model molecule for selective hydrogenation, where the aim is to only hydrogenate the C=C bond while the carbonyl O=C bond remains intact [101]. Recently, the adsorption of isophorone on Ag(001) supported MgO thin film with Au clusters was studied by means of STM methods [102]. The molecules were found to attach to the edges of 2D Au clusters, while the interiors of the clusters remained pristine. By using voltage pulses, the molecules could be removed from the cluster edges, enabling the study of the same cluster with and without the adsorbates. This revealed a systematic shift of the unoccupied QW states of the clusters towards the Fermi energy when the edges were decorated with isophorone. Further, the easy removability indicates that the molecules interact weakly with Au. Motivated by this experimental work, we investigated the adsorption of isophorone on Ag supported MgO thin film with a single Au adatom and an Au stripe modeling the edge of a large 2D Au cluster.

3.5.1   Isophorone in a vacuum

In this section, isophorone is studied in vacuum. Since the molecule exhibits keto-enol tautomerism, the keto form and two enol forms shown in Figure 3.24**a)** are considered. Two molecules are tautomers of each other if they have the same atoms but the bonds between the atoms are different and the molecules easily change from the higher energy one to the lower energy one in the gas phase. If one of the tautomers is a ketone (i.e. contains a carbonyl group O=C) and one is an enol (i.e. has a hydroxyl group OH at the end of C=C double bond), the molecule is said to exhibit keto-enol tautomerism. The studied enol forms are the extended and vinylogous enol. A H atom from C6

shown in Figure 3.24**a**) is moved to the carbonyl O in the extended enol, while the methyl group in C3 is replaced by a methylene group and the carbonyl O with an OH group in the vinylogous enol. The single and double bonds have different C-C distances which are about 1.35 Å for the double bonds, while the single bonds are between 1.45 and 1.55 Å. The keto isophorone is the most stable in gas-phase being about 0.5 (0.64) eV more stable than the vinylogous (extended) enol. The KS orbitals for the keto isophorone are displayed in Figure 3.24**b**) showing that the HOMO state is localized around the O=C1 bond while the HOMO-1 state is at the double bond between C2 and C3.
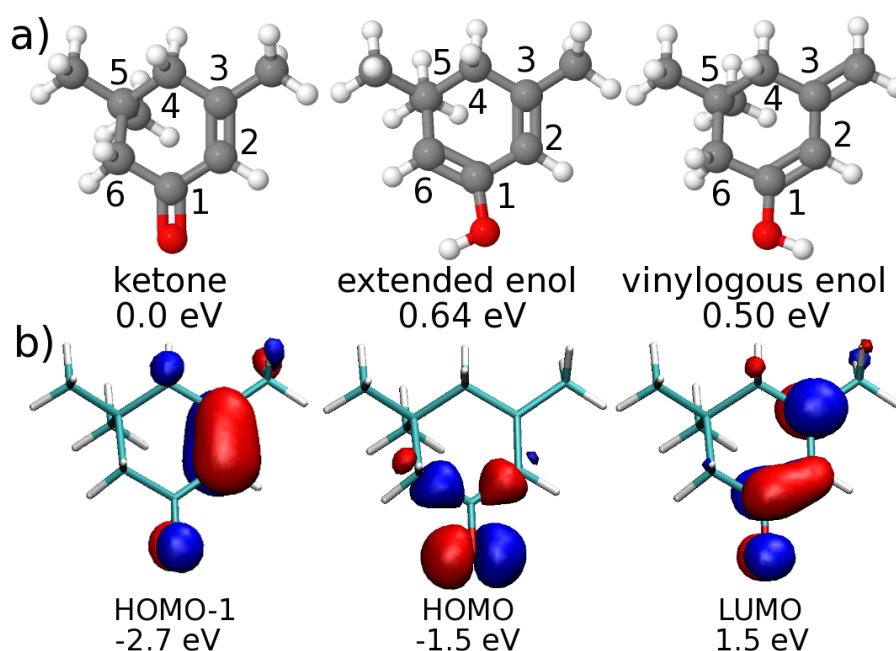

Figure 3.24: **a**)Optimized geometries for keto, extended enol, and vinylogous enol forms of isophorone in a vacuum. The relative stabilities of the structures are given with the keto isophorone being the most stable. The double bonds are shown with two sticks and the C atoms in the ring are numbered for easier reference. The C atoms are dark grey and the rest of the colors are as in Figure 3.11. **b**) KS orbitals for keto isophone. The orbital energies are given with respect to the Fermi level that is set to zero.

Table 3.5: The Bader charges of the O, C1, and H atom in the OH group for the enol forms with $|q_{rest}|$ as the maximum absolute charge of the remaining atoms in the molecule in $|e|$.

	q_{C1}	q_O	q_H	$|q_{rest}|$
keto	0.95	-1.10		0.08<
extended enol	0.46	-1.10	0.56	0.09<
vinylogous enol	0.47	-1.08	0.55	0.11<

The isophorone molecules are covalently bonded structures, which is reflected in the

Bader charges of the atoms as seen from Table 3.5. Most of the atoms in all three forms of the molecule are neutral, but the O=C1 bond in the keto form, together with the H-O and O-C1 bonds in the enol tautomers, are polar. This is indicated by the nonzero Bader charges of these atoms. The interaction with the positive end of the polar O=C1 bond in the keto isophorone might be prevented by a steric hindrance from the neighbouring C atoms, contrary to the enol forms where the H in the OH group does not have a similar hindrance. Therefore, the keto and enol tautomers will have different adsorption behaviour in the presence of negatively charged species.
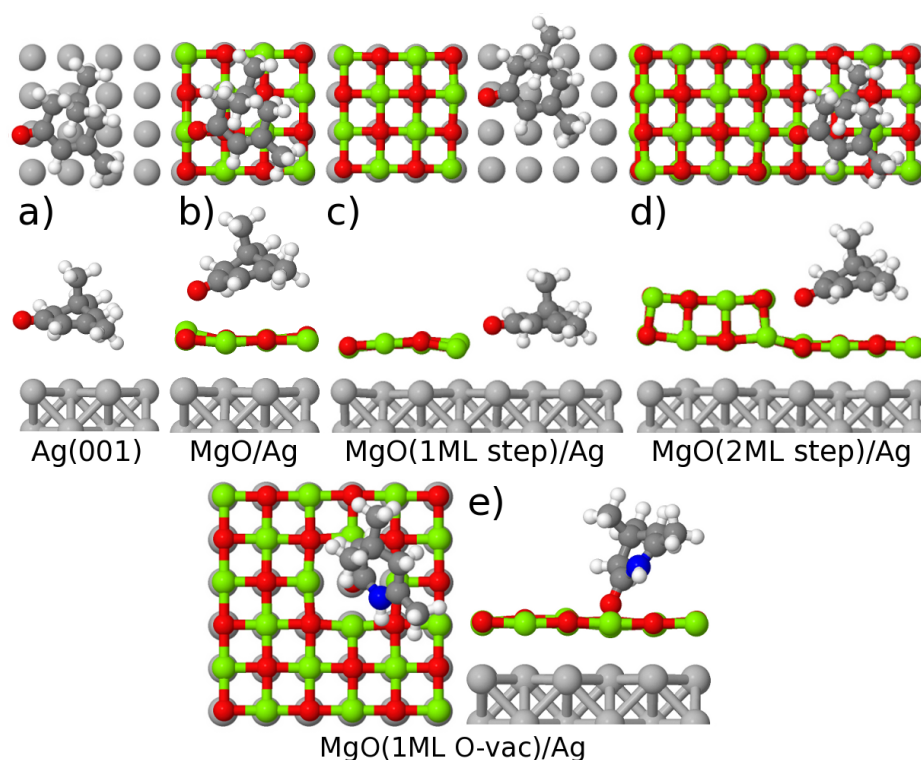
3.5.2   Keto isophorone on MgO/Ag(001)

Figure 3.25: The relaxation geometries of keto isophorone on different sites of a MgO/Ag(001) surface. The C2 atom is shown in blue when it is double bonded to both C1 and C3 otherwise the C atoms are dark grey while the rest of the colors are as in Figure 3.11.

The analysis of isophorone adsorption on MgO/Ag(001) is focused on the keto form since it is 0.6 eV more stable than the extended enol on the same site. Even though the terrace sites are the most common, the MgO/Ag(001) surface has defect sites with different properties from an ideal MgO/Ag terrace. Examples of these defect sites are the MgO steps and the MgO-Ag interface, where the bare Ag(001) support is exposed. In this section, adsorption of keto isophorone is considered on five different

Table 3.6: The adsorption energy in eV and Bader charge in |e| for isophorone.

	E_{ads}	$q_{isophorone}$
Ag(001)	-0.53	-0.06
MgO/Ag(001)	-0.69	-0.20
MgO(1ML step)/Ag(001)	-1.21	-0.14
MgO(2ML step)/Ag(001)	-1.37	-0.26
MgO(1ML O-vac)/Ag(001)	-1.17	-0.93

slab models, each addressing a different adsorption site on a realistic MgO/Ag(001) thin film surface. Two terrace sites and two step sites are considered in addition to a terrace with an oxygen vacancy. The relaxation geometries on different sites are shown in Figure 3.25, with Table 3.6 giving the corresponding adsorption energies. In order to account for vdW interactions, the BEEF XC functional is used.

Calculations indicate that isophorone physisorbs on all studied surface sites except the O vacancy as seen from the long bonding distances, lack of charge transfer, and mildly exothermic adsorption energies consistent with physisorption. While the vdW interactions are similar on all adsorption sites, the molecule has some site selectivity due to an attractive electrostatic interaction between the surface cations and the polar O=C1 bond. The isophorone prefers the step sites where the cations are more exposed and the negative carbonyl oxygen can be oriented towards them. The adsorption becomes more exothermic in the order of Ag(001) terrace (3.25a)), MgO/Ag(001) terrace (3.25b)), MgO-Ag interface (3.25c)), and step between one and two Ag supported MgO layers (3.25d)). The pristine Ag(001) surface has no Mg cations, and therefore, there is no electrostatic stabilization. However, the most stable adsorption is on the MgO/Ag(001) step, where there are two cations near the carbonyl oxygen in the relaxed structure. The simple electrostatic picture does not hold for the O vacancy (3.25e)) since the binding on the oxygen vacancy is due to a chemical interaction. Contrary to the terrace and step sites, the molecule obtains one electron and a double bond is formed between the C1 and C2 atoms at an oxygen vacancy. Since the density of O vacancies on MgO thin films is small [10] and they are mainly at the step edges, [103–105], the dominant adsorption sites are the MgO steps.

3.5.3   Au and isophorone on MgO/Ag(001)

As discussed in the previous section, the site selectivity in the isophorone adsorption on MgO/Ag(001) is due to electrostatic interactions. Since the vdW forces will affect all tautomers roughly equally, the differences between the keto and enol species will be due to differences in electrostatics. As discussed previously, the positive charge in the enol isophorone is behind a significant steric hindrance from C atoms in the
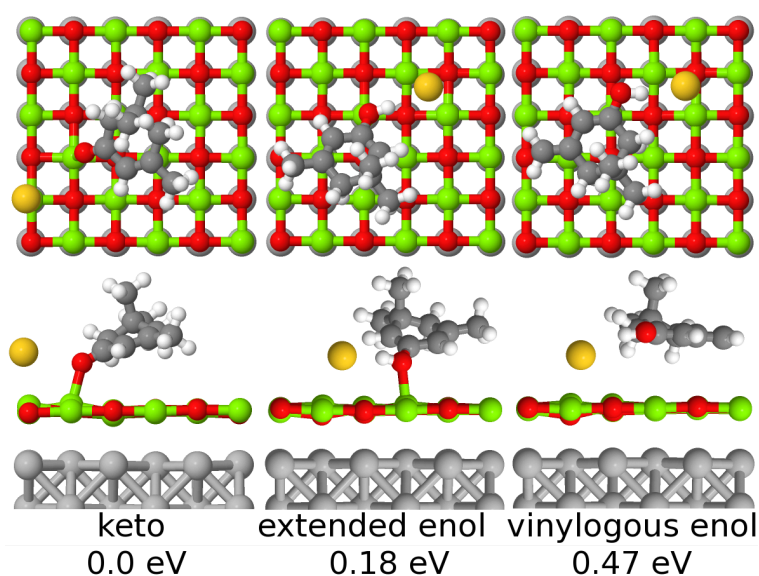
Figure 3.26: The optimal relaxation geometries of isophorone on MgO/Ag(001) with an Au adatom. The relative stabilities of the structures are given with the structure with keto form being the most stable. The colors are as in Figure 3.25.

ring. Thus, if the keto form does not interact chemically with Au, then only the enol form will be electrostatically attracted to the anionic Au adatoms. The chemical interaction between Au and keto species is deemed unlikely based on multiple vacuum calculations with Au and keto isophorone. The Au atom and keto species are fixed to approximately the same plane, and the bonding angles and distances are varied. No significant binding between Au and keto isophorone was observed even when the charge state of Au was changed to +1 or -1. A surface calculation with keto species and an Au adatom on MgO/Ag(001) displays only the expected electrostatic repulsion and no chemical bonding. During structure optimization, the total energy of the Au and keto form on MgO/Ag(001) surface closely follows a $1/d^2$ behaviour with respect to the Au-carbonyl O distance. In the most stable adsorption geometry shown in Figure 3.26, the Au-carbonyl O distance is 3.7 Å.

The difference in relative stability between keto and extended enol is significantly different for the surface with an Au adatom when compared with the bare surface. While the surface with the keto species was 0.6 eV more stable without the Au adatom, the enol form is only 0.18 eV less stable with Au adatom compared with the keto isophorone. The adsorption geometries with Au adatom for the tautomers are shown in Figure 3.26. The precence of Au atom stabilizes the enol isophorone with an attractive Au-H interaction. This electrostatic stabilization, however, is not strong enough to overcome the energy difference between keto and enol forms in vacuum and thus the surface with keto isophorone has the lowest energy. Interestingly, the vinylogous enol is not as stable on the Au/MgO/Ag(001) surface as the extended enol even though the

vinylogous enol is more stable in a vacuum. The increased stability of the extended
form over the vinylogous enol is due to added stabilization from the short distance
between the carbonyl O and a surface cation. The vinylogous form has two H atoms
in the C6 atom causing steric repulsion that prevents the electrostatic stabilization
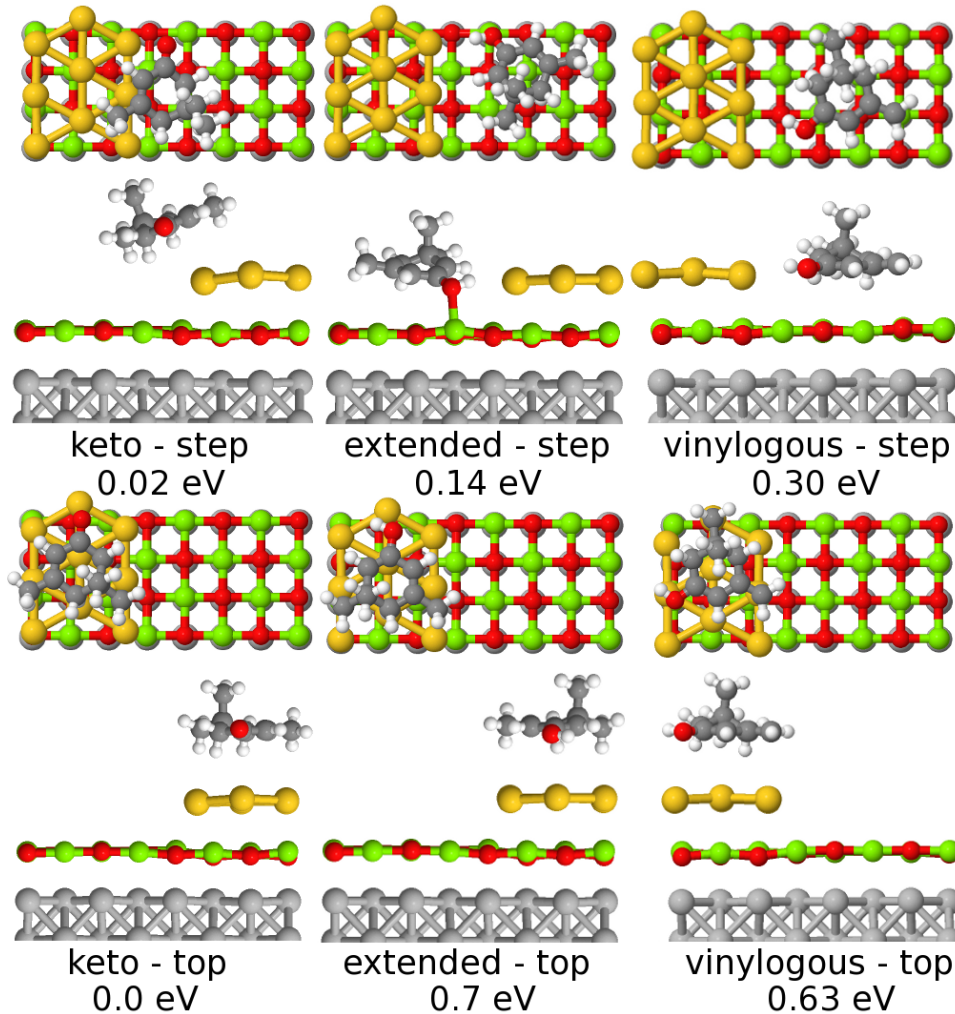between the carbonyl O and a surface cation.

Figure 3.27: The relaxation geometries of isophorone on MgO/Ag(001) with an Au stripe. The
colors are as in Figure 3.25.

As discussed in the Introduction, Au atoms form large clusters with negatively charged
edges on the MgO/Ag(001) surface. The size of these clusters can be up to hundreds
of atoms, and this is beyond the scope of DFT calculations with a reasonable compu-
tational cost. Instead, an Au stripe model shown in Figure 3.27 is used to study the
adsorption at the edges and on top of a large Au cluster. The Au stripe has similar
Au-Au distances and charging behaviour as large Au clusters [52]. The edge atoms in

the Au stripe should produce electrostatic interaction with isophorone comparable to that of a large cluster. The negatively charged edges of the stripe give a stabilizing effect on the enol forms, while the keto isophorone has no site selectivity between the top and edge of the Au stripe. The experimentally observed adsorption behaviour with decorated edges and clean cluster tops could be explained by the site selectivity of enol isophorone. However, in a similar manner to the single Au adatom case, the energy difference between the keto and enol forms in vacuum means that the surface with keto isophorone is lower in energy than the surface with an enol tautomer even though keto species gets no additional electrostatic stabilization from the presence of Au.

While the surfaces with keto species remain energetically favored over the surfaces with enol isophorone, the energy differences between them are very small. Therefore, based on the calculated energies, the presence of enol isophorone at the Au cluster edges is at least thermodynamically possible. The kinetic effects can be important, but are not studied here. The site selectivity observed in experiments could be explained by the electrostatic interaction between the enol species and the cluster edge. However, the keto form does not display similar site selectivity since only the MgO steps bind the keto tautomer beyond vdW forces. The exact mechanism for the formation of enol tautomers on the surface remain beyond the scope of this study, however.

4 Summary and outlook

In this thesis, the adsorption of gold together with oxygen, water, and isophorone was studied on modified oxide surfaces using a computational DFT approach. The considered surfaces were CaO doped with high valence dopants and MgO thin films grown on an Ag(001) support. The main result was that these modified oxides can have analogous adsorption characteristics, which can be rationalized using a Born-Haber cycle devised from an acid-base interaction concept. The introduction of electronegative species such as Au and O_2 on both surfaces resulted in a charge transfer to the adsorbate from the high valence dopant in the doped oxides, and from the metal support in the thin films. The charge transfer was accompanied with increased surface adhesion of the adsorbate species, leading to the planar growth of Au clusters.

A simple electrostatic picture was sufficient to rationalize the stronger binding of Au and O_2 on the high valence doped CaO with the most important stabilization occurring between the dopant and the oxide matrix. The interaction between the charged adsorbate and dopant quickly decays with increasing film thickness, while the stabilization from the O^{2-} anions adjacent to the positively charged dopant remained nearly fixed with film thickness up to six oxide monolayers between the adsorbate and dopant. Further, since the dominant stabilization was between the dopant and the oxide lattice, other electronegative species should also be more stable on the doped oxide, provided that the charge transfer from the dopant to the adsorbate occurs. A correlation was found between the redox energy and the third ionization potential of the dopant and it could be potentially used to prepare surfaces that bind electronegative species with a desired strength. This should be advantageous in the future design of catalysts.

On thin film surfaces, the electrostatic interaction between the charged adsorbate and support was highly important for the ML thick films, but it was insufficient in explaining the long ranged thin film effects on adsorbates. The increase in the film thickness beyond a monolayer gives a reduction in the work function of the surface, which was correlated with a more exothermic redox reaction in the adsorption of electronegative species such as Au and OH. The modified Born-Haber cycles presented for both the doped oxides and thin films are easily generalizable and could potentially provide more insight into other systems not studied in this work.

The molecular adsorption of water on an Ag(001) supported MgO thin film was further stabilized with Au on the surface due to an electrostatic interaction between anionic

59

Au and the polar H-O bond in water. The origin of the stabilization was traced to electrostatics, since water adsorption on a bulk MgO surface was not affected by the presence of Au. The Au adatoms were neutral on bulk MgO, and did not interact similarly with the polar molecule as the adatoms on the thin films. The dissociation products of water preferred the adsorption on top of the Au adatom for the bulk MgO surface and Ag(001) supported films with thickness from one to three monolayers. An exception was the OH adsorption on a ML thick film, where adsorption on top of Au was nearly isoenergetic to the adsorption on a bridge site between two Mg cations.

Interestingly, the adsorption on top of Au became more exothermic with increasing film thickness for both the H and OH species. This reversal of the more common trend of less exothermic adsorption with thicker films was explained by the formation of neutral AuH and AuOH species. Further, a correlation between H and OH adsorption energies was established for films with varying thickness. This correlation should extend to other adsorbates, provided that they form neutral species with Au. The correlations between adsorption energies can be utilized in the search for optimal catalysts. The dissociative adsorption was less exothermic than the molecular adsorption for all studied film thicknesses, which indicates that Au/MgO/Ag(001) does not spontaneously dissociate water.

The step sites dominate the adsorption of isophorone on the MgO/Ag(001) surface. The molecule was physisorbed on steps and terraces, but an additional electrostatic stabilization between more exposed step cations and a polar O=C bond in the molecule made the step sites energetically preferred over the terrace sites. Isophorone did not interact chemically with Au, as was seen from multiple calculations with Au and isophorone in vacuum. Due to lack of chemical interaction, the coadsorption of Au and isophorone was characterized by electrostatics. The keto form of isophorone had a repulsive interaction with an Au adatom, while the enol forms interacted attractively with an Au adatom. The change in the adsorbate-adsorbate interaction was due to a change in the polarity of the bonds between the tautomers. The lack of stabilizing interaction for the keto isophorone suggests that the experimentally observed site preference towards the edges of Au clusters might be due to the presence of enol isophorone.

Charged species caused distortions in the highly ionic oxide lattice. These distortions were related to the charges of the atoms, and could be used to identify the charges in different parts of the system. Multiple correlations were found between the charge states and positions of the atoms. These correlations can be used to estimate the charges of atoms without explicitly considering the electron density. A simple model proposed for explaining these correlations can potentially be used to identify similar correlations in other systems as well.

References

[1] H.-J. Freund, H. Kuhlenbeck, and V. Staemmler. *Oxide surfaces*. Rep. Prog. Phys. **59**, 283 (1996).

[2] M. Bäumer and H.-J. Freund. *Metal deposits on well-ordered oxide films*. Prog. Surf. Sci. **61**, 127 (1999).

[3] H.-J. Freund and G. Pacchioni. *Oxide ultra-thin films on metals: new materials for the design of supported metal catalysts*. Chem. Soc. Rev. **37**, 2224 (2008).

[4] N. Nilius. *Properties of oxide thin films and their adsorption behavior studied by scanning tunneling microscopy and conductance spectroscopy*. Surf. Sci. Rep. **64**, 595 (2009).

[5] L. Giordano and G. Pacchioni. *Oxide Films at the Nanoscale: New Structures, New Functions, and New Materials*. Acc. Chem. Res. **44**, 1244 (2011).

[6] G. Pacchioni and H. Freund. *Electron Transfer at Oxide Surfaces. The MgO Paradigm: from Defects to Ultrathin Films*. Chem. Rev. **113**, 4035 (2013).

[7] K. Honkala. *Tailoring oxide properties: An impact on adsorption characteristics of molecules and metals*. Surf. Sci. Rep. **69**, 366 (2014).

[8] K. Honkala, A. Hellman, and H. Grönbeck. *Water Dissociation on MgO/Ag(100): Support Induced Stabilization or Electron Pairing?*. J. Phys. Chem. C **114**, 7070 (2010).

[9] S. Schintke, S. Messerli, M. Pivetta, F. Patthey, L. Libioulle, M. Stengel, A. De Vita, and W.-D. Schneider. *Insulator at the Ultrathin Limit: MgO on Ag(001)*. Phys. Rev. Lett. **87**, 276801 (2001).

[10] S. Schintke and W.-D. Schneider. *Insulators at the ultrathin limit: electronic structure studied by scanning tunnelling microscopy and scanning tunnelling spectroscopy*. J. Phys.: Condens. Matter **16**, R49 (2004).

[11] E. W. McFarland and H. Metiu. *Catalysis by Doped Oxides*. Chem. Rev. **113**, 4391 (2013).

[12] H.-J. Freund, S. Shaikhutdinov, and N. Nilius. *Model Studies on Heterogeneous Catalysts at the Atomic Scale*. Top. Catal. **57**, 822 (2014).

[13] N. Nilius and H.-J. Freund. *Activating Nonreducible Oxides via Doping*. Acc. Chem. Res. **48**, 1532 (2015).

[14] N. Nilius. *Exploring routes to tailor the physical and chemical properties of oxides via doping: an STM study*. J. Phys. Condens. Matter **27** (2015).

[15] Y. Cui, X. Shao, M. Baldofski, J. Sauer, N. Nilius, and H.-J. Freund. *Adsorption, Activation, and Dissociation of Oxygen on Doped Oxides*. Angew. Chem. Int. Ed. **52**, 11385 (2013).

[16] Y. Cui, X. Shao, S. Prada, L. Giordano, G. Pacchioni, H.-J. Freund, and N. Nilius. *Surface defects and their impact on the electronic structure of Mo-doped CaO films: an STM and DFT study*. Phys. Chem. Chem. Phys. **16**, 12764 (2014).

[17] P. Goodman. *Current and future uses of gold in electronics*. Gold Bull. **35**, 21 (2002).

[18] T. W. Ellis. *The future of gold in electronics*. Gold Bull. **37**, 66 (2004).

[19] G. C. Bond. *Gold: a relatively new catalyst*. Cat. Rev. - Sci. Eng. **72**, 5 (2002).

[20] G. C. Bond. *Chemisorption and Reactions of Small Molecules on Small Gold Particles*. Molecules **17**, 1716 (2012).

[21] G. J. Hutchings. *Catalysis by gold*. Catal. Today **100**, 55 (2005).

[22] G. J. Hutchings and M. Haruta. *A golden age of catalysis: A perspective*. Appl. Catal. A Gen. **291**, 2 (2005).

[23] G. Bond. *The early history of catalysis by gold*. Gold Bull. **41**, 235 (2008).

[24] B. Nkosi, N. Coville, and G. Hutchings. *Vapor phase hydrochlorination of acetylene: Correlation of catalytic activity of supported metal chloride catalysts*. Appl. Catal. **43**, 33 (1988).

[25] B. Nkosi, N. Coville, G. Hutchings, M. Adams, J. Friedl, and F. Wagner. *Hydrochlorination of acetylene using gold catalysts: A study of catalyst deactivation*. J. Catal. **128**, 366 (1991).

[26] B. Nkosi, M. Adams, N. Coville, and G. Hutchings. *Hydrochlorination of acetylene using carbon-supported gold catalysts: A study of catalyst reactivation*. J. Catal. **128**, 378 (1991).

[27] M. Haruta, T. Kobayashi, H. Sano, and N. Yamada. *Novel Gold Catalysts for the Oxidation of Carbon Monoxide at a Temperature far Below 0 $\deg C$*. Chem. Lett. **16**, 405 (1987).

[28] G. C. Bond and D. T. Thompson. *Catalysis by Gold*. Catal. Today **41**, 5 (1999).

[29] H. Häkkinen and U. Landman. *Gas-Phase Catalytic Oxidation of CO by Au2-*. J. Am. Chem. Soc. **123**, 9704 (2001).

[30] N. Lopez and J. K. Nørskov. *Catalytic CO Oxidation by a Gold Nanoparticle: A Density Functional Study*. J. Am. Chem. Soc. **124**, 11262 (2002).

[31] L. D. Socaciu, J. Hagen, T. M. Bernhardt, L. Wöste, U. Heiz, H. Häkkinen, and U. Landman. *Catalytic CO Oxidation by Free Au2-: Experiment and Theory*. J. Am. Chem. Soc. **125**, 10437 (2003).

[32] O. Lopez-Acevedo, K. A. Kacprzak, J. Akola, and H. Häkkinen. *Quantum size effects in ambient CO oxidation catalysed by ligand-protected gold clusters*. Nat. Chem. **2**, 329 (2010).

[33] M. Okumura, S. Nakamura, S. Tsubota, T. Nakamura, M. Azuma, and M. Haruta. *Chemical vapor deposition of gold on Al2O3, SiO2, and TiO2 for the oxidation of CO and of H2*. Catal. Lett. **51**, 53 (1998).

[34] I. X. Green, W. Tang, M. Neurock, and J. T. Yates. *Spectroscopic Observation of Dual Catalytic Sites During Oxidation of CO on a Au/TiO2 Catalyst*. Science **333**, 736 (2011).

[35] H. Häkkinen, S. Abbet, A. Sanchez, U. Heiz, and U. Landman. *Structural, Electronic, and Impurity-Doping Effects in Nanoscale Chemistry: Supported Gold Nanoclusters*. Angew. Chem. Int. Ed. **42**, 1297 (2003).

[36] J. Guzman and B. C. Gates. *Catalysis by Supported Gold: Correlation between Catalytic Activity for CO Oxidation and Oxidation States of Gold*. J. Am. Chem. Soc. **126**, 2672 (2004).

[37] B. Yoon, H. Häkkinen, U. Landman, A. S. Wörz, J.-M. Antonietti, S. Abbet, K. Judai, and U. Heiz. *Charging Effects on Bonding and Catalyzed Oxidation of CO on Au8 Clusters on MgO*. Science **307**, 403 (2005).

[38] P. Pyykkö. *Relativistic effects in structural chemistry*. Chem. Rev. **88**, 563 (1988).

[39] P. Pyykkö and J. P. Desclaux. *Relativity and the periodic system of elements*. Acc. Chem. Res. **12**, 276 (1979).

[40] L. A. Cole and J. P. Perdew. *Calculated electron affinities of the elements*. Phys. Rev. A **25**, 1265 (1982).

[41] H. Häkkinen, M. Moseler, and U. Landman. *Bonding in Cu, Ag, and Au Clusters: Relativistic Effects, Trends, and Surprises*. Phys. Rev. Lett. **89**, 033401 (2002).

[42] X.-G. Xiong, W.-H. Xu, J. Li, and P. Pyykkö. *Aspects of bonding in small gold clusters*. International Journal of Mass Spectrometry **354–355**, 15 (2013).

[43] G. Pacchioni, L. Giordano, and M. Baistrocchi. *Charging of Metal Atoms on Ultrathin* MgO/Mo(100) *Films*. Phys. Rev. Lett. **94**, 226104 (2005).

[44] K. Honkala and H. Häkkinen. *Au adsorption on regular and defected thin MgO(100) films supported by Mo*. J. Phys. Chem. C **111**, 4319 (2007).

[45] M. Sterrer, T. Risse, U. Martinez Pozzoni, L. Giordano, M. Heyde, H.-P. Rust, G. Pacchioni, and H.-J. Freund. *Control of the charge state of metal atoms on thin MgO films*. Phys. Rev. Lett. **98**, 096107 (2007).

[46] X. Shao, S. Prada, L. Giordano, G. Pacchioni, N. Nilius, and H.-J. Freund. *Tailoring the Shape of Metal Ad-Particles by Doping the Oxide Support*. Angew. Chem. Int. Ed. **50**, 11525 (2011).

[47] X. Shao, N. Nilius, and H.-J. Freund. *Crossover from two- to three-dimensional gold particle shapes on CaO films of different thicknesses*. Phys. Rev. B **85**, 115444 (2012).

[48] L. Giordano, G. Pacchioni, J. Goniakowski, N. Nilius, E. D. L. Rienks, and H.-J. Freund. *Charging of Metal Adatoms on Ultrathin Oxide Films: Au and Pd on FeO/Pt(111)*. Phys. Rev. Lett. **101**, 026102 (2008).

[49] D. Ricci, A. Bongiorno, G. Pacchioni, and U. Landman. *Bonding trends and dimensionality crossover of gold nanoclusters on metal-supported MgO thin films*. Phys. Rev. Lett. **97**, 036106 (2006).

[50] M. Walter, P. Frondelius, K. Honkala, and H. Häkkinen. *Electronic structure of MgO-Supported au clusters: Quantum dots probed by scanning tunneling microscopy*. Phys. Rev. Lett. **99**, 096102 (2007).

[51] X. Lin, N. Nilius, H.-J. Freund, M. Walter, P. Frondelius, K. Honkala, and H. Häkkinen. *Quantum Well States in Two-Dimensional Gold Clusters on MgO Thin Films*. Phys. Rev. Lett. **102**, 206801 (2009).

[52] X. Lin, N. Nilius, M. Sterrer, P. Koskinen, H. Häkkinen, and H.-J. Freund. *Characterizing low-coordinated atoms at the periphery of MgO-supported Au islands using scanning tunneling microscopy and electronic structure calculations*. Phys. Rev. B **81**, 153406 (2010).

[53] C. Stiehler, Y. Pan, W.-D. Schneider, P. Koskinen, H. Häkkinen, N. Nilius, and H.-J. Freund. *Electron quantization in arbitrarily shaped gold islands on MgO thin films*. Phys. Rev. B **88**, 115415 (2013).

[54] V. Simic-Milosevic, M. Heyde, X. Lin, T. König, H.-P. Rust, M. Sterrer, T. Risse, N. Nilius, H.-J. Freund, L. Giordano, and G. Pacchioni. *Charge-induced formation of linear Au clusters on thin MgO films: Scanning tunneling microscopy and density-functional theory study*. Phys. Rev. B **78**, 235429 (2008).

[55] P. Frondelius, H. Häkkinen, and K. Honkala. *Adsorption and activation of O-2 at Au chains on MgO/Mo thin films*. Phys. Chem. Chem. Phys. **12**, 1483 (2010).

[56] J. Mortensen, L. Hansen, and K. Jacobsen. *Real-space grid implementation of the projector augmented wave method*. Phys. Rev. B **71**, 035109 (2005).

[57] J. Enkovaara, C. Rostgaard, J. J. Mortensen et al. *Electronic structure calculations with GPAW: a real-space implementation of the projector augmented-wave method*. J. Phys.: Condens. Matter **22**, 253202 (2010).

[58] J. P. Perdew, K. Burke, and M. Ernzerhof. *Generalized gradient approximation made simple*. Phys. Rev. Lett. **77**, 3865 (1996).

[59] V. I. Anisimov, J. Zaanen, and O. K. Andersen. *Band theory and Mott insulators: Hubbard U instead of Stoner I*. Phys. Rev. B **44**, 943 (1991).

[60] V. I. Anisimov, A. I. Poteryaev, M. A. Korotin, A. O. Anokhin, and G. Kotliar. *First-principles calculations of the electronic structure and spectra of strongly correlated systems: dynamical mean-field theory*. J. Phys.: Condens. Matter **9**, 7359 (1997).

[61] S. L. Dudarev, G. A. Botton, S. Y. Savrasov, C. J. Humphreys, and A. P. Sutton. *Electron-energy-loss spectra and the structural stability of nickel oxide: An LSDA+U study*. Phys. Rev. B **57**, 1505 (1998).

[62] J. Wellendorff, K. T. Lundgaard, A. Møgelhøj, V. Petzold, D. D. Landis, J. K. Nørskov, T. Bligaard, and K. W. Jacobsen. *Density functionals for surface science: Exchange-correlation model development with Bayesian error estimation*. Phys. Rev. B **85**, 235149 (2012).

[63] K. Burke. *Perspective on density functional theory*. J. Chem. Phys. **136**, 150901 (2012).

[64] A. D. Becke. *Perspective: Fifty years of density-functional theory in chemical physics*. J. Chem. Phys. **140**, 18A301 (2014).

[65] A. Zangwill. *A half century of density functional theory*. Phys. Today **68**, 34 (2015).

[66] P. Hohenberg and W. Kohn. *Inhomogeneous Electron Gas*. Phys. Rev. **136**, 864 (1964).

[67] W. Kohn and L. J. Sham. *Self-Consistent Equations Including Exchange and Correlation Effects*. Phys. Rev. **140**, 1133 (1965).

[68] W. Kohn. *Nobel Lecture: Electronic structure of matter - wave functions and density functionals*. Rev. Mod. Phys. **71**, 1253 (1999).

[69] R. van Leeuwen. *Density functional approach to the many-body problem: key concepts and exact functionals*. Adv. Quantum Chem. **43**, 25 (2003).

[70] U. von Barth. *Basic Density-Functional Theory - an Overview*. Phys. Scripta **109**, 9 (2004).

[71] C. Klaus. *A bird's-eye view of density-functional theory*. Braz. J. Phys. **36**, 1318 (2006).

[72] R. M. Martin. *Electronic structure - basic theory and practical methods*. Cambridge university press, UK (2004).

[73] J. Perdew and S. Kurth. *Density functionals for non-relativistic coulomb systems*, volume 500 of *Lecture Notes in Physics*. Springer Berlin Heidelberg (1998).

[74] D. M. Ceperley and B. J. Alder. *Ground State of the Electron Gas by a Stochastic Method*. Phys. Rev. Lett. **45**, 566 (1980).

[75] B. Himmetoglu, A. Floris, S. de Gironcoli, and M. Cococcioni. *Hubbard-corrected DFT energy functionals: The LDA+U description of correlated systems*. Int. J. Quantum Chem. **114**, 14 (2014).

[76] K. Berland, V. R. Cooper, K. Lee, E. Schröder, T. Thonhauser, P. Hyldgaard, and B. I. Lundqvist. *van der Waals forces in density functional theory: a review of the vdW-DF method*. Rep. Prog. Phys. **78**, 066501 (2015).

[77] P. E. Blöchl. *Projector augmented-wave method*. Phys. Rev. B **50**, 17953 (1994).

[78] P. Blöchl, C. Först, and J. Schimpl. *Projector augmented wave method:ab initio molecular dynamics with full wave functions*. Bull. Mater. Sci. **26**, 33 (2003).

[79] R. Bader. *Atoms in Molecules: A quantum theory*. Oxford University Press, New York (1990).

[80] W. Tang, E. Sanville, and G. Henkelman. *A grid-based Bader analysis algorithm without lattice bias*. J. Phys.: Condens. Matter **21**, 084204 (2009).

[81] E. Sanville, S. D. Kenny, R. Smith, and G. Henkelman. *An improved grid-based algorithm for Bader charge allocation*. J. Comp. Chem. **28**, 899 (2007).

[82] G. H. A. Arnaldsson and H. Jónsson. *A fast and robust algorithm for Bader decomposition of charge density*. Comput. Mater. Sci. **36**, 254 (2006).

[83] Y. Cui, C. Stiehler, N. Nilius, and H.-J. Freund. *Probing the electronic properties and charge state of gold nanoparticles on ultrathin MgO versus thick doped CaO films*. Phys. Rev. B **92**, 075444 (2015).

[84] F. Stavale, X. Shao, N. Nilius, H.-J. Freund, S. Prada, L. Giordano, and G. Pacchioni. *Donor Characteristics of Transition-Metal-Doped Oxides: Cr-Doped MgO versus Mo-Doped CaO*. J. Am. Chem. Soc. **134**, 11380 (2012).

[85] H. Metiu, S. Chrétien, Z. Hu, B. Li, and X. Sun. *Chemistry of Lewis Acid–Base Pairs on Oxide Surfaces*. J. Phys. Chem. C **116**, 10439 (2012).

[86] http://www.webelements.com.

[87] R. D. Shannon. *Revised effective ionic radii and systematic studies of inter-atomic distances in halides and chalcogenides*. Acta. Cryst. **32**, 751 (1976).

[88] S. Prada, L. Giordano, and G. Pacchioni. *Charging of Gold Atoms on Doped MgO and CaO: Identifying the Key Parameters by DFT Calculations*. J. Phys. Chem. C **117**, 9943 (2013).

[89] M. Haruta. *Catalysis: Gold rush*. Nature **437**, 1098 (2005).

[90] A. Hellman, S. Klacar, and H. Grönbeck. *Low Temperature CO Oxidation over Supported Ultrathin MgO Films*. J. Am. Chem. Soc. **131**, 16636 (2009).

[91] P. Frondelius, H. Häkkinen, and K. Honkala. *Formation of Gold(I) Edge Oxide at Flat Gold Nanoclusters on an Ultrathin MgO Film under Ambient Conditions*. Angew. Chem. Int. Ed. **49**, 7913 (2010).

[92] M. A. Henderson. *The interaction of water with solid surfaces: fundamental aspects revisited*. Surf. Sci. Rep. **46**, 1 (2002).

[93] M. A. Brown, E. Carrasco, M. Sterrer, and H.-J. Freund. *Enhanced Stability of Gold Clusters Supported on Hydroxylated MgO(001) Surfaces*. J. Am. Chem. Soc. **132**, 4064 (2010).

[94] M. A. Brown, Y. Fujimori, F. Ringleb, X. Shao, F. Stavale, N. Nilius, M. Sterrer, and H.-J. Freund. *Oxidation of Au by Surface OH: Nucleation and Electronic Structure of Gold on Hydroxylated MgO(001)*. J. Am. Chem. Soc. **133**, 10668 (2011).

[95] M. Sterrer and H.-J. Freund. *Towards Realistic Surface Science Models of Heterogeneous Catalysts: Influence of Support Hydroxylation and Catalyst Preparation Method*. Catal. Lett. **143**, 375 (2013).

[96] S. Kouva, J. Andersin, K. Honkala, J. Lehtonen, L. Lefferts, and J. Kanervo. *Water and carbon oxides on monoclinic zirconia: experimental and computational insights*. Phys. Chem. Chem. Phys. **16**, 20650 (2014).

[97] R. Hacquart and J. Jupille. *Hydrated MgO smoke crystals from cubes to octahedra*. Chem. Phys. Lett. **439**, 91 (2007).

[98] J. Carrasco, F. Illas, and N. Lopez. *Dynamic Ion Pairs in the Adsorption of Isolated Water Molecules on Alkaline-Earth Oxide (001) Surfaces*. Phys. Rev. Lett. **100**, 016101 (2008).

[99] J. Jung, H.-J. Shin, Y. Kim, and M. Kawai. *Controlling water dissociation on an ultrathin MgO film by tuning film thickness*. Phys. Rev. B **82**, 085413 (2010).

[100] Z. Ding and S. Meng. *Promote water photosplitting via tuning quantum well states in supported metal clusters*. Phys. Rev. B **86**, 045455 (2012).

[101] M. Pisarek, M. Łukaszewski, P. Winiarek, P. Kędzierzawski, and M. Janik-Czachor. *Selective catalytic hydrogenation of isophorone on Ni−Al alloy modified with Cr*. Mater. Chem. Phys. **114**, 774 (2009).

[102] C. Stiehler, F. Calaza, W.-D. Schneider, N. Nilius, and H.-J. Freund. *Molecular Adsorption Changes the Quantum Structure of Oxide-Supported Gold Nanoparticles: Chemisorption versus Physisorption*. Phys. Rev. Lett. **115**, 036804 (2015).

[103] C. D. Valentin, R. Ferullo, R. Binda, and G. Pacchioni. *Oxygen vacancies and peroxo groups on regular and low-coordinated sites of MgO, CaO, SrO, and BaO surfaces*. Surf. Sci. **600**, 1147 (2006).

[104] M. Sterrer, M. Heyde, M. Novicki, N. Nilius, T. Risse, H.-P. Rust, G. Pacchioni, and H.-J. Freund. *Identification of Color Centers on MgO(001) Thin Films with Scanning Tunneling Microscopy*. J. Phys. Chem. B **110**, 46 (2006).

[105] T. König, G. H. Simon, H.-P. Rust, G. Pacchioni, M. Heyde, and H.-J. Freund. *Measuring the Charge State of Point Defects on MgO/Ag(001)*. J. Am. Chem. Soc. **131**, 17544 (2009).